The Pennsylvania State University

The Graduate School

Department of Electrical Engineering

OBSERVATIONS OF ATMOSPHERIC WATER VAPOR USING RAMAN LIDAR TECHNIQUES

A Thesis in

Electrical Engineering

by

Ronnie S. Harris

Submitted in Partial Fulfillment
of the Requirements
for the Degree of

Master of Science

May 1996

_____

Ronnie S. Harris

We approve the thesis of Ronnie S. Harris

Date of Signature

Charles R. Philbrick Professor of Electrical Engineering Thesis Advisor	
Timothy J. Kane Assistant Professor of Electrical Engineering	
Larry C. Burton Professor of Electrical Engineering Head of the Department of Electrical Engineering	

ABSTRACT

Raman lidar has become a well-established technique to obtain water vapor profiles. Measurements of the atmospheric distributions of water vapor have been made with the LAMP lidar (Laser Atmospheric Measurement Program) during the 1995 Case I measurement program on Wallops Island, VA. The history of the development of methods used to obtain water vapor measurements is briefly reviewed. Scattering mechanisms used by LAMP lidar are summarized as a basis for obtaining atmospheric distributions of water vapor. A description of the LAMP lidar, its system parameters, and the analysis procedure used to determine water vapor profiles is presented. A correction applied to the water vapor measurements to account for the attenuation due to the wavelength dependence of molecular (Rayleigh) scattering is provided. A correction needed for the tropospheric ozone absorption in the Hartley band for the UV channels is also provided. Simultaneous measurements obtained from the vibrational Raman technique at night using visible and UV channels were compared to validate the Raman technique for the UV channel. A comparison between the visible and UV channels produced an overall correlation coefficient of 0.96. Nighttime profiles from the surface to 5 km and daytime vertical profiles from the surface to about 1 km are displayed to illustrate results from LAMP lidar. Useful daytime measurements are expected up to 2.5 km from the LAMP instrument. Suggestions for improvements in obtaining water vapor profiles are made for future experiments.

TABLE OF CONTENTS

LIST OF FIGURES

LIST OF TABLES

ACKNOWLEDGMENT

First of all, I would like to thank my thesis advisor, C.R. Philbrick, for all of his valuable support and guidance. I would also like to thank T. Kane for his many useful suggestions in the preparation of this thesis. I also appreciate the efforts of F. Balsinger for the many hours that he helped me with this thesis.

Next, I would like to thank all the people in the PSU lidar group and ARL faculty for their contributions to this thesis, including: G. Pancoast, T. Petach, R. Smith, G. Evanisko, S. Mathur, S. Rajan, M. O'Brien, B. Durbin, and T. Stevens.

CHAPTER 1

Introduction

Snow, hail, ice, rain, clouds, and vapor are all forms of water that can exist in the atmosphere. Water vapor, one of the most variable components in the atmosphere, is measured in order to provide insight to the Earth's hydrologic cycle and global climate. The hydrologic cycle is the global transport of the Earth's water in its many forms [1]. Changes in the Earth's climate are due to the tremendous amount of energy transported over global scales as water vapor evaporates and condenses. When water vapor evaporates, latent heat is transferred into the atmosphere and when it condenses, sensible heat is extracted by the atmosphere, thereby, regulating the Earth's temperature worldwide. All of these factors, including the fact that water vapor is a selective absorber of terrestrial and solar radiation, make water vapor a major influence on the Earth's climatic system. Figure 1 is a diagram of the Earth's hydrological cycle. It gives emphasis to the important role that evaporation, **E** , advection of water vapor, **Q**, and the precipitation of water, **P,** play in the Earth's atmosphere.

The largest concentration of atmospheric water vapor is found in the lower troposphere. As the altitude increases, the concentration of water vapor decreases making it difficult to measure at higher altitudes. Thus, there are very few observations of water vapor in the stratosphere and even fewer in the mesosphere. Water vapor in the troposphere participates as one of the "greenhouse" gases by absorbing and trapping the radiation that is remitted by the Earth in the 5 to 8 μm region and other parts infrared of the spectrum. As shown in Figure 2, water vapor also absorbs much of the Sun's direct

radiation in many portions of the infrared spectrum. Absorption and emission spectra of water vapor encompass more of the infrared and microwave regions than any other atmospheric molecule. Thus, water vapor has a strong influence on the Earth's energy budget. An understanding of the spatial and temporal distribution of water vapor in the atmosphere is needed in order to model many of Earth's atmospheric processes.

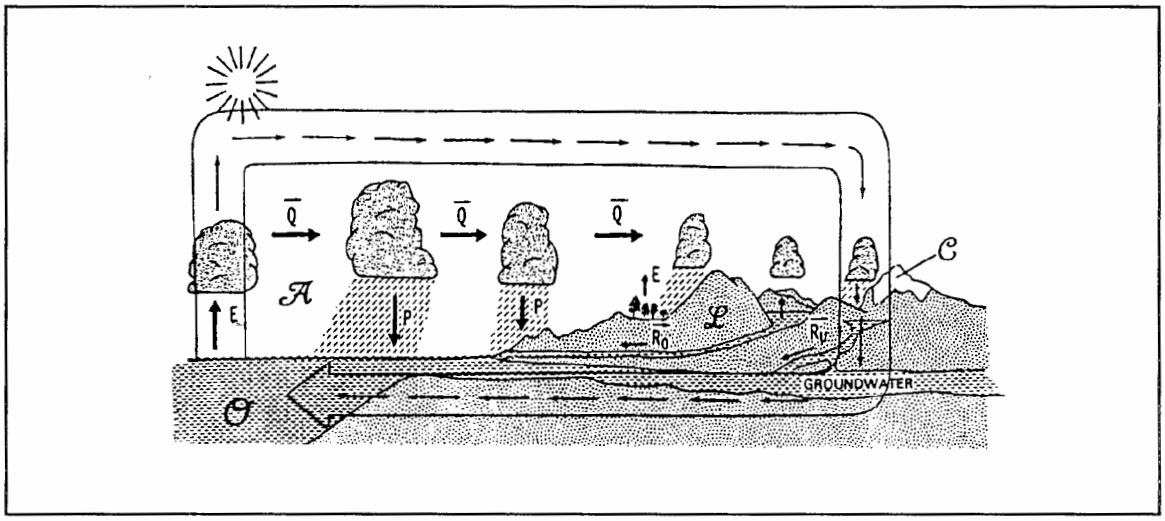

Figure 1. Diagram of the earth's hydrological cycle showing evaporation **E**, advection **Q**, precipitation **P**, river runoff $\mathbf{R}_0$, and underground runoff $\mathbf{R}_u$ of water in the atmosphere (Peixto and Oort, 1992 [1]).

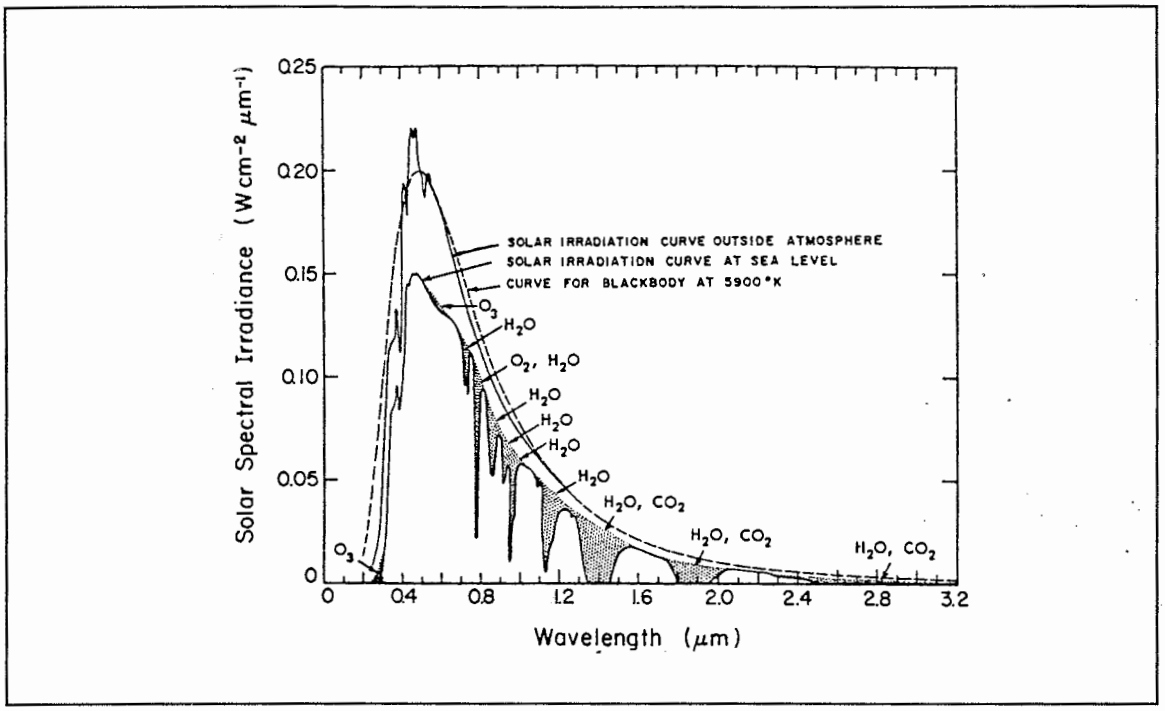

Figure 2. Plot of the spectral irradiance of direct sunlight before and after it passes through the atmosphere. The stippled regions give the atmospheric absorption of several constituents (Measures, 1984 [2]).

1.1 The Vibrational and Rotational States of Water Vapor

Each atmospheric gas has certain modes of vibration, stretch, and rotation that produce energy states that determine its absorption and emission characteristics. The vibrational and rotational energy transitions of these gases are very important in the absorption of solar radiation, especially in the infrared and microwave regions of the spectrum. The vibrational and rotational energy transitions of a molecule are determined by its molecular structure. Figure 3 shows the molecular structure of water vapor, indicating its three vibrational modes, υ_1, υ_2, and υ_3. H_2O is highly active in the infrared and microwave regions of the spectrum because of its many modes of vibrating, bending, and stretching of the molecular bonds. As shown in the figure, the configuration has an

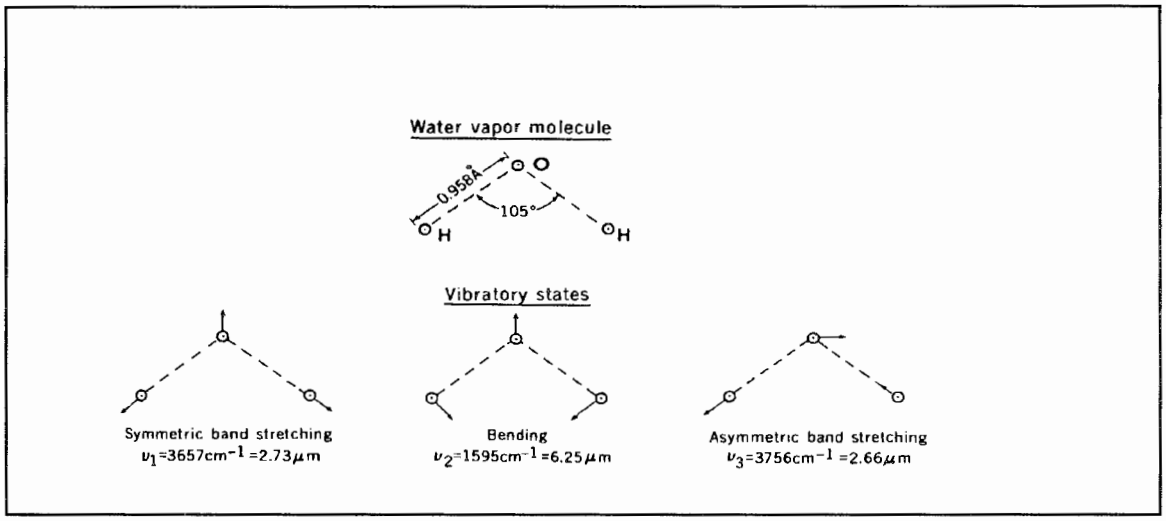

Figure 3. The structure of water vapor and its vibratory states (Peixto and Oort, 1992 [1]).

oxygen atom between hydrogen atoms which are extended on either side. At the center of its mass, the water vapor molecule has three orthogonal rotational axes with different moments of inertia.

The combination of water vapor's rotational and vibrational modes results in a very complex absorption spectrum containing many bands of thousands of lines. Water vapor has a pure rotational band, which has scattering cross sections about two orders of magnitude smaller and are lower energy than the vibrational lines, that is broadly centered at 65 μm [1]. Water vapor has many vibrational-rotational bands that are situated in the 1-8 μm region of the spectrum [1].

1.2 Methods of Measuring Water Vapor

Some of the most commonly used methods of measuring water vapor content in the atmosphere are: radiosondes, satellite observations, meteorological towers, and remote sensing instruments [3, 4, 5]. Radiosondes, meteorological towers, and in situ aircraft are some of the most popular methods of measuring water vapor. A radiosonde station includes a receiver unit, processors and program memories with antenna and peripheral connectors. Helium balloons are used to transport the radiosondes which contain sensors to measure wind speed and direction, temperature, atmospheric pressure, and relative humidity. A lithium chloride thermistor produces temperature measurements by measuring changes in current in a wire as a result of changes in temperature. The humidity sensor measures changes in current when water is absorbed by a carbon element [6]. The pressure is measured with a barometer which provides the pressure height and ground sensors are used to convert the motion of the sonde to wind speed and direction measurements, in addition to the radars that are used to track the balloon. Water vapor profiles are obtained from the radiosonde measurements of relative humidity and temperature. Although radiosondes provide good spatial resolution, they provide poor temporal resolution because the typical 3 to 4 hours rise time limits the frequency of observations [3]. Also, it is virtually impossible to obtain a true vertical profile from radiosondes because the balloons move horizontally with the background wind. Observations obtained by satellites encompass wide geographic regions, however, the measurements have poor spatial resolution and are not very accurate. On the other hand,

meteorological towers provide measurements with high temporal and altitude resolution, but they are limited in height to a few hundred meters [3].

For the past thirty years, scientists have been developing a variety of laser remote sensing instruments that measure water vapor content in the atmosphere. Laser remote sensing instruments may be used on mobile platforms, such as aircraft and helicopters, or from fixed platforms on the ground. Operation of these instruments is somewhat analogous to the operation of a radar, in that backscatter radiation provides the signal. There are several advantages involved with the use of remote sensing instruments to monitor atmospheric constituents, such as: 1) true vertical profiles can be obtained, 2) the instrument can be used to obtain measurements in a wide variety of locations, 3) successive measurements can be made at intervals of minutes, and 4) the atmosphere remains undisturbed by the measurements [3].

The first measurements of water vapor content in the atmosphere by a laser remote sensing instrument were based on differential absorption, which is known as the DIAL technique [7]. This technique is based on the principle that each species has sharp absorption lines that are unique for that molecule. The DIAL technique uses data obtained at an absorbing wavelength compared to a nearly non-absorbing wavelength to yield an integrated profile of the absorbing species.

Schotland et al. [7] was one of the first scientists to demonstrate the DIAL technique using a thermally tuned ruby laser operating in the region from 693.7 nm to 694.5 nm. Subsequently, two more temperature-tuned DIAL lasers were built, and each of these systems had the capability of obtaining nighttime measurements up to 10 km.

Subsequent, DIAL systems for measuring water vapor used CO_2 lasers operating in the 9.2 to 10.7 μm spectral region [8, 9]. Gradually, dye lasers operating in the 720 to 730 nm spectral region were used in DIAL water vapor systems [10]. Eventually, interests were shifted away from using DIAL instruments because of the disadvantages involved with the technique, such as 1) the water vapor cross section has temperature dependencies which can affect the measurement accuracy, 2) Doppler broadening from atmospheric molecules can alter the absorption profile, 3) amplified spontaneous emission (ASE) of the laser source can cause errors in the near field for dye lasers, and 4) spatially inhomogeneous aerosol distribution can give rise to measurement errors [5]. These factors require stringent control of the center wavelength and line width of the laser.

The Raman scattering lidar technique was initially tested in the late 1960's [11, 12] and was used for measurements of water vapor. It is based on the Raman shifting of the incident wavelength by vibrational energy states of the targeted species. The Raman lines associated with the first Stokes transition are used for molecules at atmospheric temperatures. The uniqueness in the spectral signature of each species means that, in practice, only one laser wavelength can be used to identify a wide variety of molecular species, simultaneously. Figure 4 summarizes the magnitude of Raman frequency shifts of several molecular species, which for water vapor is 3651.7 cm^{-1}.

Of particular interest to many scientists is the measurement of water vapor by Raman lidar systems. There are a variety of lasers sources that are used in Raman lidar systems which transmit beams with wavelengths between 248.5 nm to 694.3 nm.

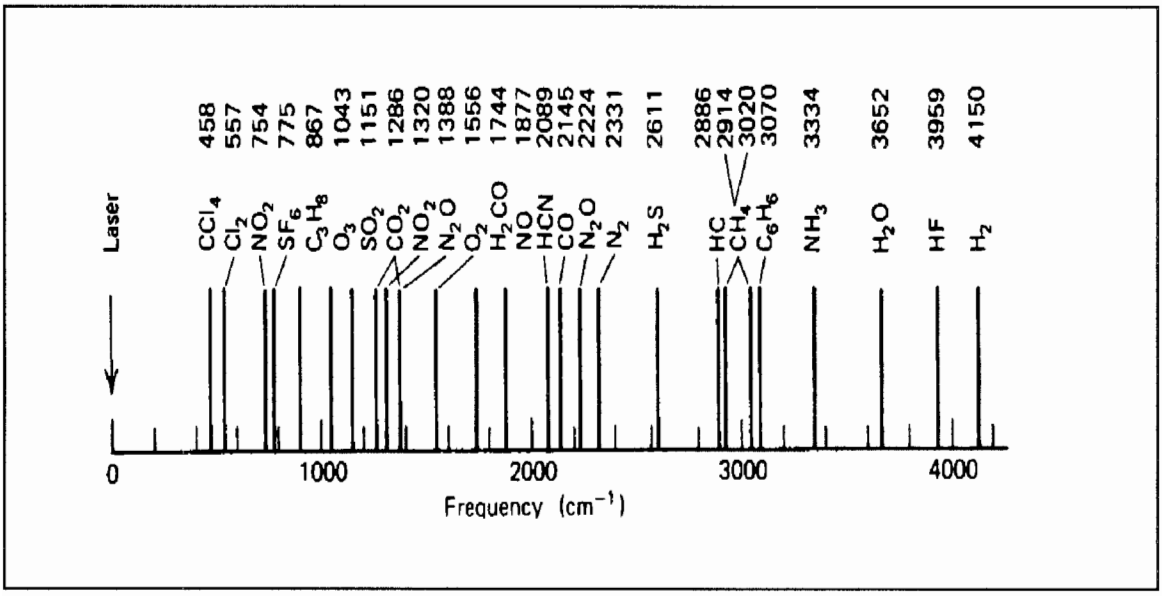

Figure 4. Frequency shifts of the Q-branch of vibrational -rotational Raman spectra of various molecular species (Measures, 1984 [2]).

Although the best wavelength to use for nighttime measurements of water vapor is between 300 nm to 350 nm, the best wavelengths for daytime measurements are between 260 - 265 nm in the spectral region [4]. For wavelengths longer than 265 nm, solar radiation interferes with the measurements and for wavelengths less than 265 nm, ozone attenuation increases [4].

In 1969, Raman lidar measurements of the spatial distribution of water vapor in the atmosphere were obtained. Melfi et al. (1969) and Cooney (1970) performed experiments with Raman lidars using high powered frequency doubled ruby lasers. They realized the importance of making a ratio of their water vapor returns with nitrogen in order to obtain more accurate results. However, the quantity and accuracy of these early measurements were poor. By comparing their Raman lidar profiles to radiosonde measurements, they were able to determine that lidar could provide an estimate of water

vapor which was in general agreement [12].

Interest in Raman lidar technique was low during the 1970's and early 1980's as the DIAL technique became more popular. However, because of the complexity and errors of the DIAL technique, the interests in the Raman lidar technique for measuring water vapor were revived in the mid-1980's as high power Nd:YAG lasers became available. By 1985, several advancements in remote sensing technology had been made. For instance, Melfi et al. (1985) began to use a frequency tripled Nd:YAG laser and narrowband filters to select the Raman scattering wavelength of interest and to reduce background skylight [12].

A lidar which utilizes a XeF laser with a transmitting wavelength of 351 nm has been developed by scientists at NASA Goddard Space Flight Center (GSFC) [13]. Since 1985, the GSFC Raman lidar has experienced several modifications and upgrades. The photon counting capability of the system's photomultiplier tubes assists in making long-range operations possible. The water vapor measurements of the GSFC Raman lidar have been used for comparisons with other Raman lidar systems and with satellite measurements and microwave radiometers [4].

The LAMP lidar is a multi-wavelength Rayleigh/Raman lidar system. It was developed at the Pennsylvania State University to study the vertical structure and properties of atmospheric water vapor. LAMP transmits the second (532 nm) and fourth (266nm) harmonics of a Nd:YAG laser into the atmosphere and measures the returns at the water vapor frequency shifts of these two lines. The third harmonic (355 nm) can be used instead of the fourth harmonic by changing the a few components in the laser, energy

monitor, and detector. The measurements obtained from LAMP have been compared to measurements from radiosondes in order to establish that the Raman lidar technique is a useful tool for measuring water vapor [14]. A description of the LAMP lidar can be found in section 2.3 (see references [14, 15, 16]).

A Raman lidar system with scanning capabilities is being developed by Penn State University. The WAVE-LARS or Water and Aerosol Variability Environment- Lidar And Radar Sounder contains a new volume scanning lidar and 94 GHz radar and a fixed position Rayleigh/Raman lidar. The combination of LARS's volume scanning radar and its Rayleigh/ Raman lidar provides unique measurements of the structure and dynamics of the atmosphere. The WAVE-LARS lidar will be used to obtain properties of cirrus clouds, study cloud formations, obtain water vapor and temperature profiles, study optical scattering properties of aerosols, and locate regions of multiple scattering [17].

Improvements on the Raman lidar systems gave scientists the opportunity to obtain higher temporal and spatial resolutions. However, those Raman lidar measurements were restricted to nighttime operations. Daytime operations are made difficult because of the high intensity background level due to the daytime sky radiance. One solution to this problem is to operate in the solar blind region of the spectrum (between 230 and 300 nm). In this region, stratospheric ozone absorbs the solar radiation. Renaut et al. (1980) and Petrti et al. (1982) used multiwavelength Raman lidars that operated in the solar blind region to measure atmospheric water vapor [2]. The limitation in this region is that the laser transmitted beam is attenuated by molecular scattering. The Penn State LAMP lidar uses the solar blind region by transmitting the 4th harmonic of the Nd:YAG laser at a

wavelength of 266 nm which provides Raman shifted returns from H_20 at 295 nm and N_2 at 284 nm. These wavelengths allow the daytime measurements of water vapor concentrations at altitudes above 2 km.

1.3 Outline to Thesis

Water vapor measurement techniques of the LAMP lidar system will be described in this thesis. It begins with an introduction on the background and theory of water vapor's meteorological significance and optical properties. A description of methods used for measuring water vapor is given, followed by a description of basic lidar principles and the scattering processes involved in lidar measurements. The Penn State LAMP lidar system is described and measurements of the water vapor mixing ratio are presented along with corrections for the attenuation due to molecular scattering and ozone absorption. An analysis of error propagation in the data is also presented. Finally, water vapor profiles are presented from nighttime and daytime operations that were performed at Wallops Island. The thesis concludes with a discussion on the best technique for obtaining water vapor profiles and improvements that could be made for future experiments.

CHAPTER 2

Theory of Lidar Techniques

2.1 Lidar Principles of Operation

Lidar (Light Detecting and Ranging) has provided an alternate and more powerful means to help man investigate the environment. Laser remoting sensing can profile atmospheric parameters such as water vapor, temperature, aerosols, and cloud extinction. As discussed in the previous chapter, a variety of instruments have been developed for the same purposes, however, lidar can provide better temporal and spatial resolution than other techniques.

Lidar is similar to a radar, execpt it is applied at optical wavelengths, rather than radio wavelengths. Like monostatic weather radars, the lidar signal is transmitted into the atmosphere as a pulse of energy, and the backscattered signal is monitored. The return signal of the lidar may be processed via a variety of different techniques. One method that may be employed is photon counting, which involves recording the current pulses of photons that are detected with a photomultiplier. The number of scattered photons received, N(z), can be calculated using the following equation,

$$N(z) = \underset{(1)}{\eta_{eff} T_A^2} \times \underset{(2)}{\frac{P_L}{hc/\lambda}} \times \underset{(3)}{\sigma_R n(z) \Delta z} \times \underset{(4)}{\frac{A_R}{4\pi z^2}}. \qquad \textbf{(1)}$$

where z is the height determined by the time delay in the backscattered signal. This

equation, known as the lidar equation, is separated into four terms. Term 1 represents the optical efficiency of the transmitted signal and transmission of the atmosphere. Term 2 describes the number of photons transmitted at the laser power. Term 3 represents the probability of photons scattering back from molecules in the illuminated volume and term 4 describes the probability of receiving a photon in the collecting telescope of collecting area A_r. Equation 1 is just one of many forms of the lidar equation. The particular form of the lidar equation used is determined by the type of lidar being analyzed. For instance, the equation for a Raman lidar may be expressed in terms of the expected power as a function of all the lidar parameters used in the four terms of the above equation, however, the cross section for the Raman scatterers and extinction on the return path will be at the Raman shifted wavelength. Equation 1 may be applied to operations of the Penn State LAMP lidar system. A description of the LAMP system is provided in section 2.3.

2.2 Optical Scattering

The signal of laser remote sensing instruments can result from several types of scattering interactions. Two of those processes are molecular scattering and aerosol scattering. Molecular scattering may be categorized by two types of processes, those that are elastic, which are described by the theory developed by Rayleigh, and inelastic, which are described by Raman scattering theory. Both elastic molecular scattering and spherical particle or aerosol scattering can be described by the theory developed by Gustav Mie [18]. Table 1 provides a description of each of these scattering processes.

Particles in the atmosphere consist of a variety of different sizes and shapes.

Scattering theory can be applied to a particular event, however, details depend on the size and shape of the scatterer. For instance, calculations that can apply to atmospheric molecules, which are much smaller than the wavelength of visible light, are described with the simple process developed by Rayleigh. Molecular scattering occurs when the electric field of the incident wave induces a dipole moment on the molecule in its path. The electric field of the incident wave causes a change in the way that charges are distributed around the molecule. Acceleration of these charges causes the particle to reemit electromagnetic radiation near the same frequency of the incident radiation. The direction of propagation may be changed and the original wavelength may be shifted by the thermal broadening or Doppler velocity of the ensemble of molecules within the scattering volume. This scattering is referred to as elastic scattering because it is scattered back at nearly the same energy and frequency. The elastic scattered radiation is known as the Cabannes line.

The backscattering cross section for Rayleigh scattering is defined by,

$$\sigma_{\pi}^{R} = \frac{\pi^2(n^2-1)^2}{N^2} \lambda^{-4}, \qquad \textbf{(2)}$$

where n is the index of refraction, λ is the wavelength of the incident light, and N is the number of scatterers [2]. As shown in Equation 2, the cross section for Rayleigh scattering has a λ^{-4} dependence which causes the cross section to be greater at shorter wavelengths. For example, the molecular scattering cross section at 355 nm is five times greater than at 532 nm.

Rayleigh Scattering 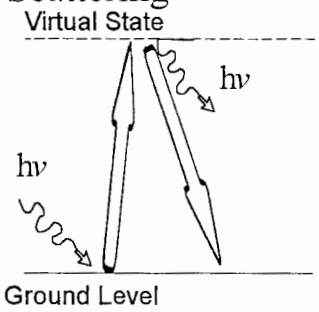   Laser radiation is scattered elastically from atoms or molecules and is observed with no change of frequency.
Mie Scattering 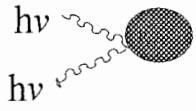   Laser radiation is elastically scattered from small particulates or aerosols (of size comparable to wavelength of radiation) and is observed with no frequency change.
Raman Scattering 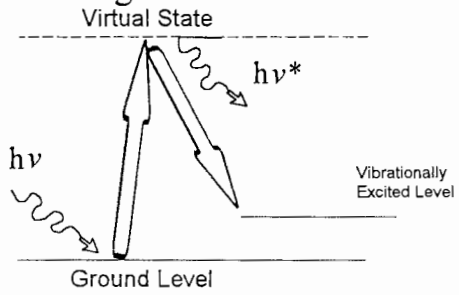   Laser radiation is scattered inelastically from molecules and observes a frequency shift that is characteristic of the molecule.

Table 1. Optical scattering mechanisms of laser remote sensing instruments (Measures, 1992[2]).

Another molecular scattering mechanism employed by laser remote sensing instruments is Raman scattering. Raman scattering is useful in atmospheric studies because it is wavelength specific for each atmospheric constituent. Raman scattering is an inelastic process, meaning that the incident radiation suffers a frequency shift that is caused by the vibrational states of a molecule. Table 1 shows a schematic representation of the Raman vibrational scattering process. A molecule absorbs an incoming photon which elevates it to a higher virtual energy level. It returns to a vibrational energy level of the molecule that is, in some cases, different from the original ground state. The photon emitted has an energy that corresponds to the difference between the incident photons and the vibrational energy level. The upward or downward frequency shift [18] can be described by the following equations,

$$f_{-}=f_{o}-f' \qquad f_{+}=f_{o}-f' \tag{3}$$

where f_o is the frequency of the incident radiation, f' is the frequency due to molecular motions, the transition f_- is called the 1st Stokes line (lower emitted energy), and the f_+ transition is called the 1st anti-Stokes line. The vibrational Raman scattering cross section of the 1st Stokes line for typical atmospheric molecules is three orders of magnitude less than the Rayleigh scattering cross section, while the first anti-Stokes line is typically seven orders less for molecular species at normal atmospheric temperatures. The vibrational Raman scattering technique can be used to provide unique identification of the scattering molecule.

Unlike molecular scattering, particle scattering involves particles that are comparable in size or much larger than the wavelength of the incident light. The theory developed by Mie describes scattering of light by aerosols. This theory can only be applied to particles that are spheres or ellipsoids, therefore, complex shaped aerosols are frequently assumed to be a distribution of spheres. Particle scattering theory developed by Mie explains the complex electric field arising from a plane electromagnetic wave of wavelength, λ, impinging upon a sphere with radius, r, and index of refraction, n [2, 18, 19]. The important variable of the particle theory of Mie is the size parameter,

$$x=\frac{2\pi r}{\lambda}. \tag{4}$$

The magnitude of the size parameter determines whether a Rayleigh approximation or a Mie calculation may be used. When the size parmeter is less than 0.5, scattering by the particle may be described by the theory developed by Rayleigh. Otherwise, scattering by larger particles may be described by the theory developed by Mie (if they are spherical).

Since the derivation of the scattering formulas of the Mie theory is somewhat complicated and tedious, only a few of the resulting formulas will be presented here. Two complex functions that fully describe the scattering process are the scattering amplitude functions, $S_1(\Theta)$ and $S_2(\Theta)$ [19], which are given by,

$$S_1(\Theta)=\sum_{n=1}^{\infty}\frac{2n+1}{n(n+1)}[a_n\pi_n(\cos\Theta)+b_n\tau_n(\cos\Theta)] \tag{5}$$

$$S_2(\Theta)=\sum_{n=1}^{\infty}\frac{2n+1}{n(n+1)}[a_n\tau_n(\cos\Theta)+b_n\pi_n(\cos\Theta)] \quad \textbf{(6)}$$

where $S_1(\Theta)$ and $S_2(\Theta)$ are both functions of only one angle, the scattering angle Θ. The cylindrical symmetry, which is produced by the combination of the particle spherical symmetry and the incoming radiation, eliminates any dependence that the scattered radiation may have on the azimuth angle [18]. The parameters a_n and b_n in Equations 5 and 6 are known as the Mie scattering coefficients. They are both a function of the index of refraction and size parameter of the scattering particles.

The scattering coefficients and the size parameter are very useful in determining parameters such as the backscattering efficiency, which is the significant parameter in the lidar applications. In 1908, Gustav Mie [2] determined the Mie scattering cross section to be,

$$\frac{d\sigma_M(\Theta,\phi)}{d\Omega}=\frac{\lambda^2}{4\pi^2}[i_2(\Theta,x,n)\cos^2\phi+i_1(\Theta,x,n)\sin^2\phi], \quad \textbf{(7)}$$

where i_1 and i_2 are the perpendicular and parallel intensity functions, respectively, and are related the scattering amplitude functions of Equations 5 and 6 in the following manner: $i_1 = |S_1|^2$ and $i_2 = |S_2|^2$. Figure 5 shows several plots of the intensity functions versus scattering angle for a certain particle size. The number of oscillations increases as the

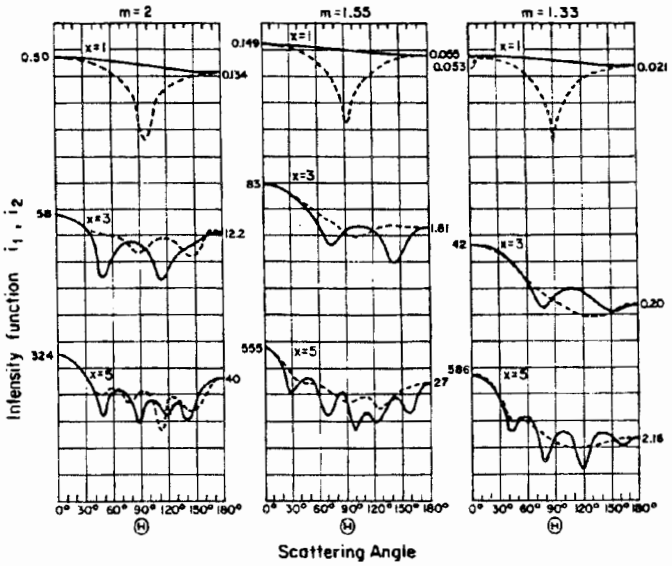

Figure 5. Scattering diagrams derived from the Mie theory for a single particle. The solid curves are for $i_1$and the dashed curves are for i_2 (Stephens, 1994 [19]).

scattering angle goes from 0° to 180° and as the size parameter increases. Also, scattering in the forward direction increases as the size parameter increases.

From the scattering cross section, the backscattering efficiency [2] can be determined to be as follows:

$$Q_{\pi}(\alpha,n) \equiv \frac{1}{\pi x^2}\frac{d\sigma_M(\Theta=\pi)}{d\Omega}. \qquad (8)$$

A plot of the backscatter efficiency versus the size parameter is shown in Figure 6. When the particles are much smaller than the wavelength of light, the graph follows the λ^{-4}

dependence explained in the Rayleigh scattering theory. However, as the particle size becomes larger than the wavelength of the incident light, the backscattering efficiency increases until x reaches a maximum, whereupon it goes into a damped oscillation. The maxima and minima experienced in the oscillations occur as a result of both the increase in particle size and the interference between the radiation scattered at the front and back surfaces of the particle. A maxima occurs when there is constructive interference and a minima occurs when there is destructive interference.

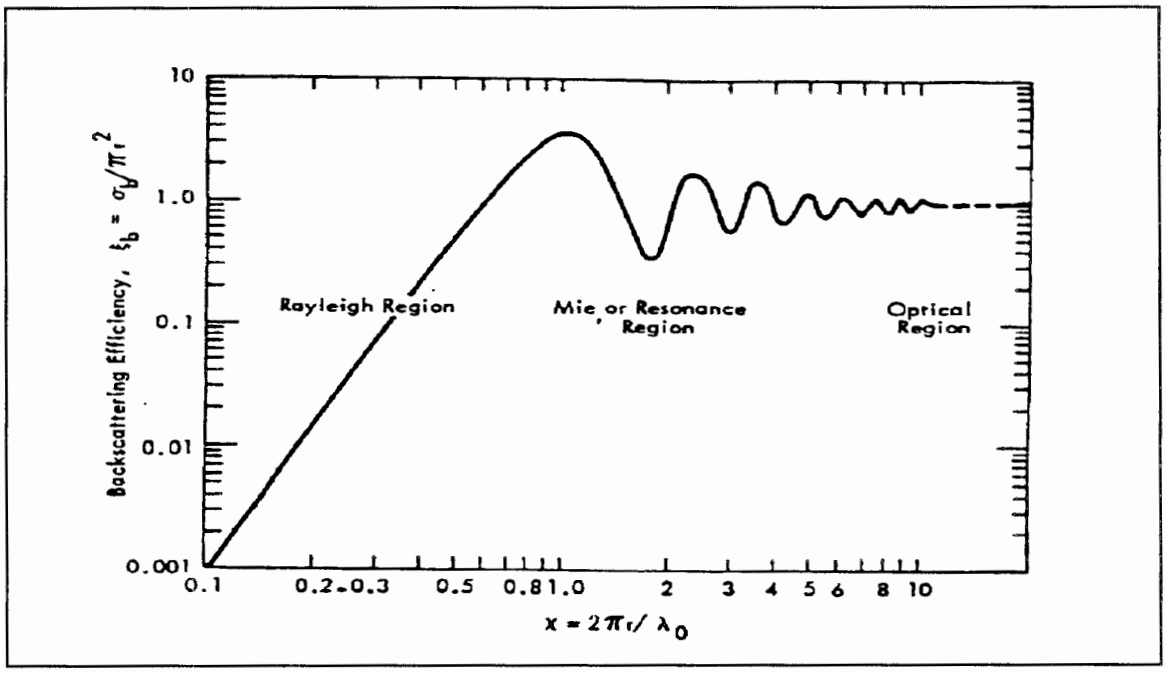

Figure 6. Backscattering Efficiency versus size parameter (Ulaby, 1981 [20])

2.3 Penn State's LAMP system

A multi-wavelength Rayleigh/Raman lidar was completed at the Pennsylvania State University in the summer of 1991. The Laser Atmospheric Measurement Program (LAMP) was developed to study the properties of the middle and lower atmosphere (0-80 km). The data collected by the LAMP lidar are used to gather information about a variety of atmospheric parameters, such as water vapor and aerosol distributions, and temperature.

As shown in Table 2 and Figure 7, the LAMP lidar utilizes a Nd:YAG laser. The Nd:YAG laser has a pulse repetition frequency of 20 Hz and a fundamental wavelength of 1064 nm. The laser beam is doubled (532 nm) and quadrupled (266 nm) by nonlinear crystals to provide a two wavelength output, it is sometimes operated with a tripler at 355 nm. The laser's maximum output energy is 1500 mJ per pulse at 1064 nm, 600 mJ per pulse at 532 nm, and 80 mJ per pulse at 266 nm. The laser beam expands through a 5X telescope and is reflected off of two hard coated mirrors that direct it into the atmosphere. Backscattered signal is collected by a f/15 Cassegrain telescope in the receiver and then collimated into a fiber optic link that transports it to the detector system. Eight detectors are used to detect the Rayleigh scattered and Raman shifted return signals. The Raman channels in the detector have narrowband filters for background noise and laser line rejection. These filters have a 0.3 nm bandwidth with 55% transmission. The current from the PMTs is converted to a voltage and is either digitized at 10 MSps in order to provide 15 meter resolution or is photon counted to provide 75 m altitude resolution [14]. The

signals from the PMT's are then averaged for one minuted intervals and recorded. LAMP's monostatic configuration allows near field as well as far field measurements.

Table 2. Penn State University LAMP Lidar parameters.

LIDAR PARAMETERS			
Power aperature product	1.5 $W \cdot m^2$		
Type	Continuum NY-82, Nd:YAG		
Wavelength (nm)	1064	532	266
Max. Pulse Energy (mJ)	1500	600	80
Typical Pulse output (mJ)	------	400	80
Bandwidth	80 MHz		
Pulse Length	6 ns		
Pulse Rate	20 Hz		
RECEIVER			
Telescope	f/15, Cassegrain		
Focal Length	609 cm		
Primary Diameter	40.6 cm		
Secondary Diameter	10.2 cm		

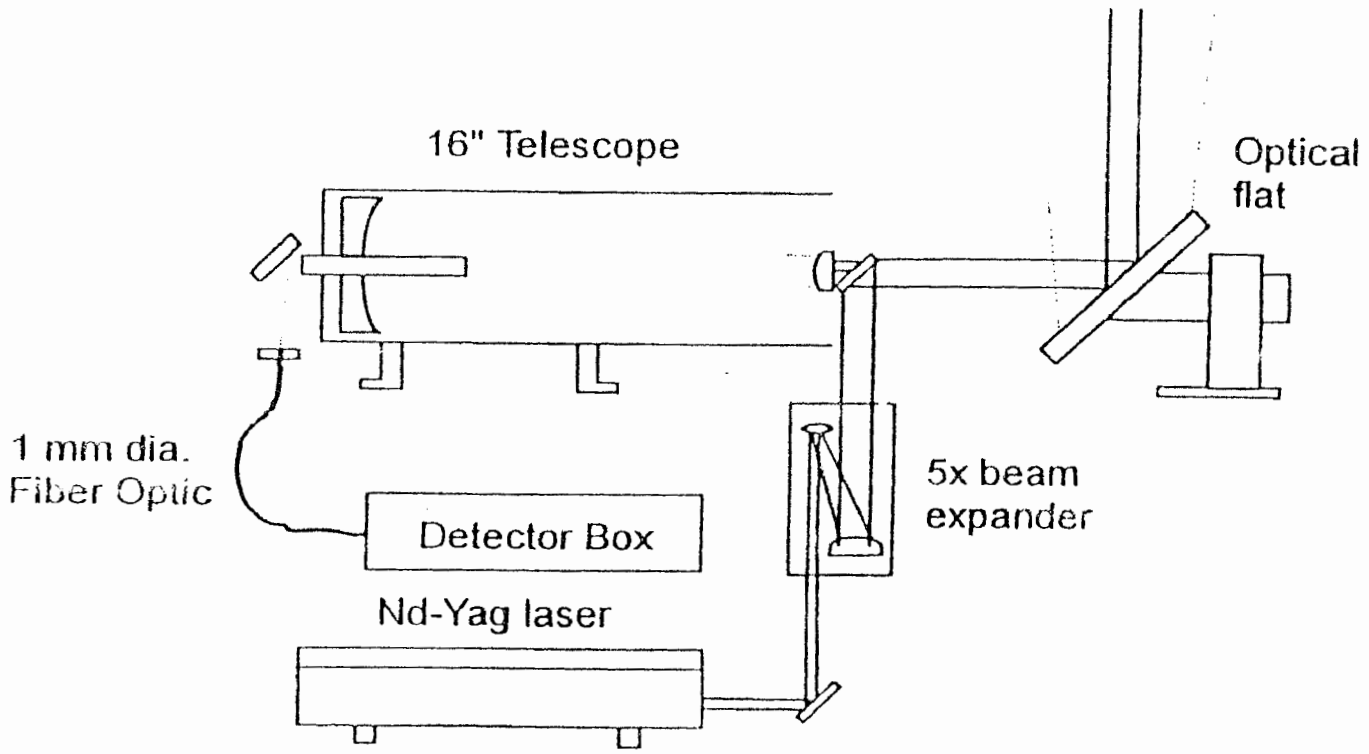

Figure 7. Schematic diagram of the Penn State LAMP lidar (Haris, 1995 [21]).

CHAPTER 3

Theory

3.1 Water Vapor mixing ratio

There are several ways to quantify and describe the water vapor content in the atmosphere. For example, it can be expressed in terms of its mass per unit volume of air, which is known as the absolute humidity, or in terms of the relative humidity, which is the ratio of the actual vapor pressure to the saturation vapor pressure. Another convenient way of expressing the water vapor content is to take the ratio of its mass to the mass of ambient dry air. This ratio is known as the mixing ratio, or specific humidity, which is given in units of grams per kilogram. The mixing ratio, r, can be expressed [22] in terms of the vapor pressure, e, and the atmospheric pressure, ρ, as follows,

$$r = 621.97 \frac{e}{(\rho - e)}. \tag{9}$$

Lidar measurements [23] of water vapor can directly measure the mixing ratio,

$$w(z) = \frac{n_{WV}(z)}{n_{dryair}(z)} \frac{M_{WV}}{M_{dryair}} = K \frac{S_{WV}(z)}{S_N(z)}, \tag{10}$$

where n is the number density, M is the molecular weight, S_{WV} is the Raman water vapor backscatter signal, S_N is the Raman nitrogen backscatter signal, and K is the calibration constant. The Raman nitrogen backscatter signal is used because nitrogen represents a constant portion of dry air and use of the ratio eliminates most of the error sources which

could affect the quantification of the result, for example, laser power variation, optical efficiency, scattering losses, and knowledge of absolute sensitivity of the detectors.

For daytime measurements, the LAMP lidar transmits at a wavelength of 266 nm and measures the vibrational Raman backscatter returns from H_20 at 295 nm and N_2 at 284 nm. The nighttime measurements use the 532 nm wavelength and measure vibrational Raman backscatter returns from H_20 at 660 nm and N_2 at 607 nm and the rotational Raman temperature returns at 528 and 530 nm. By using the ratios of signals, many of the unknown factors within the lidar equation, such as telescope form factor, absolute detector sensitivity, and transmitted power are eliminated. However, parameters that are wavelength dependent, such as molecular scattering and ozone absorption are not canceled in the ratio and must therefore be considered further in the analysis.

3.1 Attenuation Due to Molecular Scattering

As light propagates through the atmosphere, it interacts with a variety of molecular species. This interaction may take the form of scattering, where the light is redirected away from forward propagation, or absorption, which means that some of the light is absorbed by atmospheric species. The combined effects of both of these interactions is known as attenuation. In the regions of the spectrum below 0.4μm (blue to ultraviolet) attenuation is often dominated by scattering from molecules, which is proportional to atmospheric density [24]. An expression for the loss of light due to molecular scattering over a distance, z, in a scattering medium containing a number density, n, is given by,

$$I_\lambda(z) = I_{\lambda,o} e^{-\sigma \int_0^z n(z)dz}, \qquad \textbf{(11)}$$

where σ is the total Rayleigh scattering cross section [25] which is given by,

$$\sigma = \frac{(3.93\pm0.05)\times10^{-28}}{\lambda^{3.916+0.074\lambda+0.05/\lambda}} cm^2, \quad \textbf{(12)}$$

where λ is in μm, and where,

$$\tau = \sigma\int_0^z n(z)dz \quad \textbf{(13)}$$

is known as the optical depth. The optical depth is the extent to which each layer attenuates the light passing through it [24].

For altitudes below 5 km, there is an analytical way to calculate the optical depth found in Equation 13, given the temperature T_o and pressure P_o at the ground. First, assuming that temperature decreases linearly with altitude, the temperature T(z) can be expressed as follows,

$$T(z) = \alpha z + T_o, \quad \textbf{(14)}$$

where α is the lapse rate, the rate at which temperature decreases with altitude which is usually - 6.5K/km. Second, an expression for P(z), which is found below in Equation 17, is found by integrating the hydrostatic equation, Equation 16, which serves as a basis for low-altitude pressure calculations.

$$\frac{dP}{dz} = \frac{-g \cdot M}{kT(z)} \cdot P(z) \qquad \textbf{(15)}$$

$$P(z) = P_o\left(\frac{\alpha z}{T_o} + 1\right)^{\frac{-gM}{k\alpha}} \qquad \textbf{(16)}$$

Finally, by treating air as an ideal gas and by substituting the above expressions for temperature and pressure into Equation 13, the integral of the optical depth is given by,

$$\tau = \sigma\kappa(z)$$
$$\textit{where,}$$
$$\kappa(z) = \int_0^z n(z)dz = \frac{P_o}{gM}\left[1 - \left(\frac{\alpha z}{T_o} + 1\right)^{\frac{-gM}{k\alpha}}\right]. \qquad \textbf{(17)}$$

Using the expression for optical depth found in Equation 17 and assuming that molecular scattering is the only wavelength dependent attenuation, the corrected water vapor mixing ratio is given by,

$$w(z) = K\frac{S_{H_2O}(z)}{S_N(z)} e^{(\sigma_{H_2O} - \sigma_{N_2})\kappa(z)}. \qquad \textbf{(18)}$$

where the values for σ were calculated using Equation 12 and are found in Table 3. Applying this correction to the water vapor mixing ratio corrects the molecular scatter bias errors in the measurements, which for the visible channel is up to 1 % at 5km, and for the UV channels is up to 6% at 3 km.

In addition to molecular scattering, particle/ aerosol scattering causes attenuation of the of the backscattered signal, however, this contribution is difficult to estimate and its contribution is generally less significant. Figures 8 and 9 display the aerosol volume backscattering coefficient as a function of wavelength and the aerosol extinction coefficient as a function of wavelength, respectively. Figure 9 illustrates that the extinction coefficient of molecular scatterers changes substantially with the wavelength, in contrast to the that of aerosols, which shows slight changes with wavelength.

Gas	**λ (nm)**	**σ(cm^2)**
H_2O	660	2.11×10^{-27}
	407	1.52×10^{-26}
	295	5.92×10^{-26}
N_2	607	2.96×10^{-27}
	407	1.52×10^{-26}
	284	6.96×10^{-26}

Table 3. Total Rayleigh scattering cross section for N_2 and H_2O.

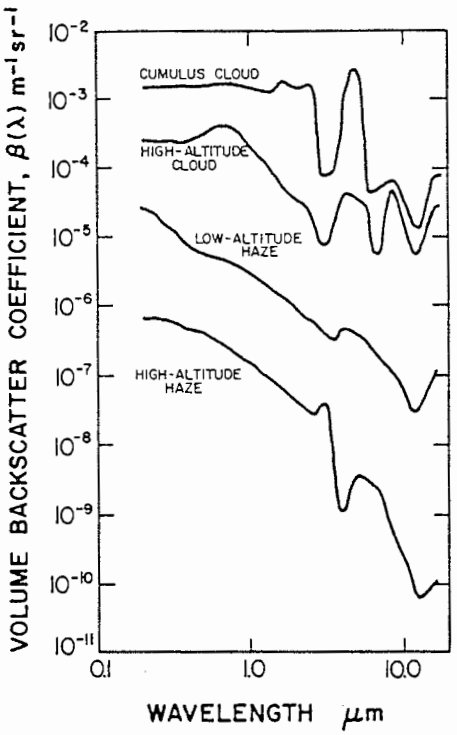

Figure 8. Aerosol volume backscattering coefficient as a function of wavelength (Measures, 1992 [2])

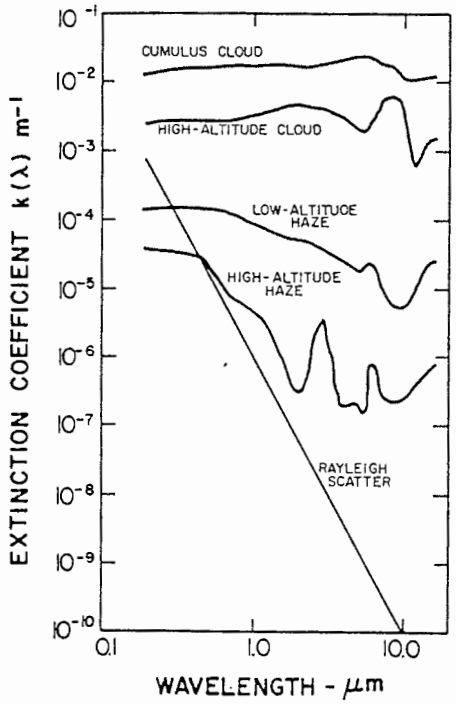

Figure 9. Aerosol extinction coefficient as a function of wavelength (Measures, 1992 [2]).

3.3 Absorption by Ozone

The greatest importance of ozone is that it is responsible for the absorption of solar radiation in the ultra-violet region of the spectrum. Ozone absorbs wavelengths over a wide region between 200 nm and 300 nm in the Hartley band and wavelengths in the Higgens band which extend to 340 nm. The region between 200 nm and 300 nm is known as the "solar blind region". Therefore, when performing daytime measurements, the solar blind region can be used to the advantage. Figure 10 displays the radiance of the Earth's atmosphere. The day radiance values are shown in the upper half of the figure. The minima centered at 250 nm is due to ozone absorption and the one centered at 150 nm is due to oxygen absorption. The advantage to operating in the solar blind region is that stratospheric ozone helps to block the high solar daytime radiance. A disadvantage to operating in the solar blind region is that tropospheric ozone also absorbs the some of the laser light, and the molecular scattering reduces the useful range.

By measuring the Raman backscatter return of O_2 at 277 nm and N_2 at 284 nm, it is possible to obtain the total ozone column density at low altitudes. Similar to the lidar expression of the water vapor mixing ratio, the expression for ozone column density is found by taking the ratio of the O_2 to the N_2 Raman backscatter signals. Applying the Beer-Lambert law to this ratio leads to the following expression [26] for ozone column density,

$$\frac{S_{O_2}}{S_{N_2}} = \frac{O_2}{N_2} e^{-C(z)}, \qquad \textbf{(19)}$$

where C(z) is the optical depth for ozone. Because the ratio of O_2 to N_2 is constant in the lower atmosphere, the contribution to the optical depth from ozone can be computed from this ratio as,

$$C(z) = (\sigma_{O_2} - \sigma_{N_2}) \int_0^z O_3 dz = \ln\left(\frac{S_{O_2}}{S_{N_2}}\right), \quad \textbf{(20)}$$

where σ is the absorption cross section, which is 484.2× 10^{-22} m^2 mol^{-1}, 285.4× 10^{-22} m^2 mol^{-1}, and 79.9× 10^{-22} m^2 mol^{-1}, for O_2, N_2, and H_2O, respectively [26]. Using the above expression , the water vapor mixing ratio can be expressed in the following form,

$$w(z) = k\frac{S_{WV}}{S_{N_2}}\left(\frac{S_{O_2}}{S_{N_2}}\right)^{\frac{\sigma_{WV}-\sigma_{N_2}}{\sigma_{N_2}-\sigma_{O_2}}} \quad \textbf{(21)}$$

where S_x are the count rates at the corresponding wavelength which have already been corrected for the losses due to molecular scattering as discussed in section 3.2.

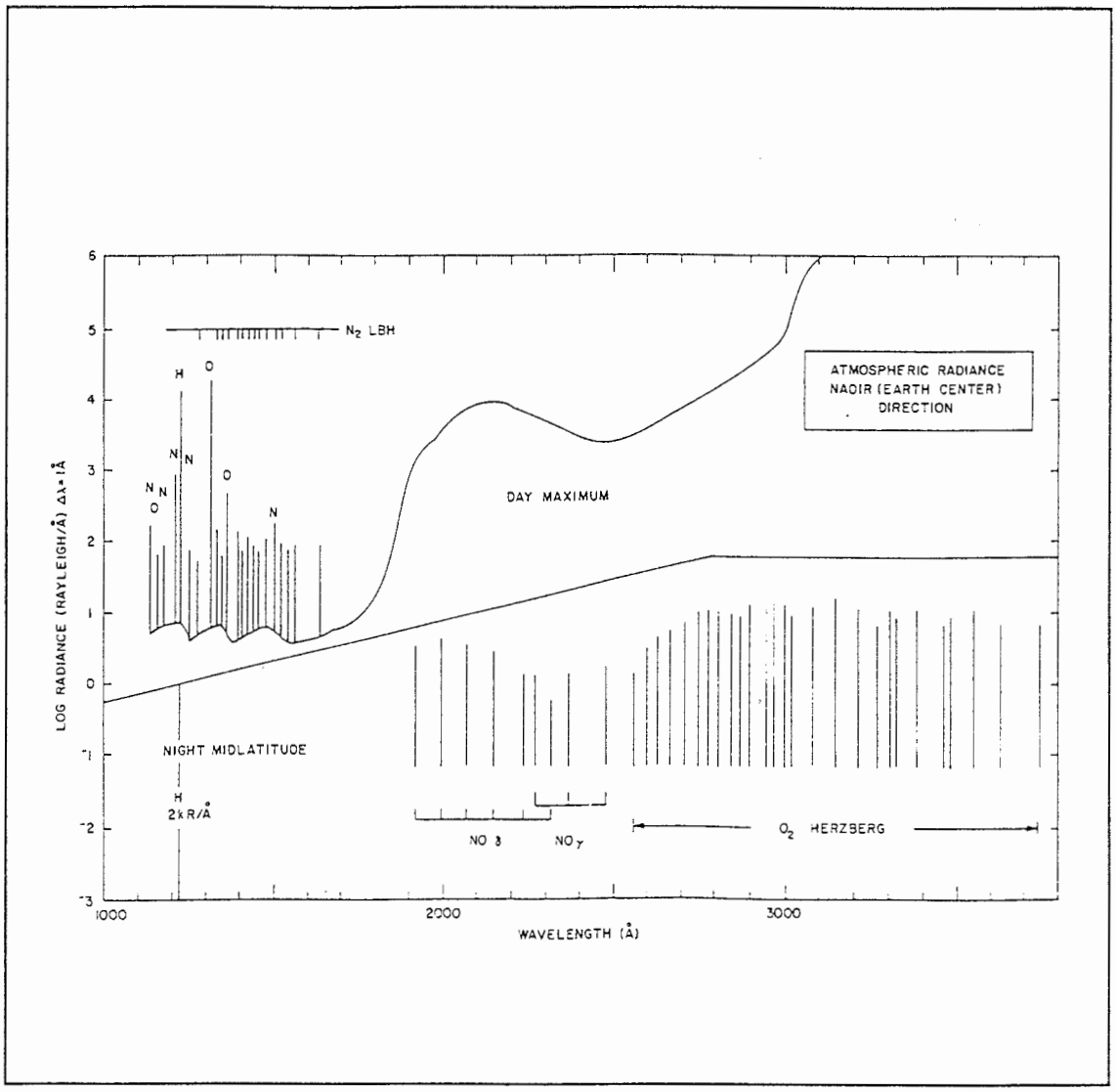

Figure 10. Atmospheric radiance in the ultraviolet region between 100 and 400 nm (Air Force, 1985 [22]).

3.4 Error Analysis

Since LAMP'S data is collected with photon counting photomultiplier tubes (PMT), Poisson statistics are used in the error analysis of the water vapor measurements. A Poisson distribution is used where the data represent the number of objects counted per unit time interval [27]. The Poisson distribution is an approximation to the binomial distribution because the number of observations is much less than the total possible number. The number of photons that are actually observed is much smaller than the number of photons scattered. The Poisson distribution may be represented as,

$$P_p = \frac{\mu^x}{x!} e^{-\mu}, \tag{22}$$

where x represents the number of objects counted per unit time interval and μ is the mean value. In Poisson statistics the standard deviation, σ, or the absolute uncertainty is equal to the square root of the mean and the relative uncertainty is given by,

$$\frac{\sigma}{x} = \frac{\sqrt{\mu}}{x}, \tag{23}$$

which is the absolute uncertainty divided by the total number of events counted.

The background measurements are sampled for thousands of bins which increases the number of values on which the statistical error is based. This results in a much smaller statistical error that is almost negligible. For each channel, the total number of background counts is summed and averaged. Thus, the count rates, S_x, at the different

channels are given as the difference between the measured signal returns and the background counts for each of the channels.

When determining the relative uncertainty of the water vapor measurements, the relative uncertainty of both the nitrogen and water vapor signals must be taken into account. Thus, the absolute uncertainty [28] for the water vapor ratio measurement is,

$$\frac{\sigma_w^2}{w^2} = \frac{\sigma_{N_2}^2}{N_2^2} + \frac{\sigma_{wv}^2}{wv^2}, \tag{24}$$

where σ_x is the absolute uncertainty, and w, n, and wv represent the water vapor ratio measurement, nitrogen measurement, and water vapor measurement, respectively. The relative uncertainty of the measurements can be used to determine the effective range of the lidar. Only data points with statistical error less than 20% are used, therefore, the profiles do not extend beyond the range of those points. As an indication of the relative uncertainty of each data point, the profiles include error bars that mark off one standard deviation on either side.

CHAPTER 4

Data and Analysis

4.1 Wallops Data

From September 9, 1995 to September 22, 1995, the LAMP lidar was included in the CASE I measurement program on Wallops Island. During the CASE I program, coincident measurements of atmospheric structure properties, water vapor, and ozone distribution were made by several different instruments. The NASA/GSFC (Goddard Space Flight Center) Raman water vapor lidar was among those instruments. Radiosondes and ozone sondes were launched by the staff at NASA Wallops. Also, the NASA LSFC aircraft water vapor experiment, LASE, had overflights on several occasions during the campaign. The data from each of these instruments is used in cooperative investigations between the various groups. Water vapor profiles obtained from the measurements of the LAMP lidar and radiosondes on September 15th, 18th, and 20th will be displayed and discussed. Those particular dates were chosen because the those days were fairly clear with low wind speeds.

4.2 Calibration of the Lidar

As shown in Equation 10, the water vapor mixing ratio is determined from the ratio of the Raman water vapor and nitrogen return signals. The calibration constant, K, can be obtained via two methods. One method uses optical transmission characteristics

and the cross section of water vapor relative to that of nitrogen [13]. This method is not used very often because of the difficulty involved in determining optical characteristics of the lidar system. Vaughan et. al (1988) utilized this method and obtained calibration constants with a 12% uncertainty [13].

Another method of determining the calibration constant is to use the water vapor measurements of a coincident radiosonde. The uncalibrated lidar profile is compared with a profile from a balloon sonde. Each lidar range bin produces a ratio of the balloon water vapor with the uncalibrated lidar value. The calibration constant is the weighted average of those ratios. There are several factors that cause uncertainty in the calibration constant when using this method, such as: 1) the balloon makes instantaneous measurements at each altitude, in contrast to the lidar which averages its values over a given interval of time, 2) the balloon drifts with the wind, therefore the measurements between the lidar and the balloon are not exactly common volume, and 3) the measurements between the two instruments are not exactly concurrent [11]. Figure 11 maps the course of a balloon after it was released and it provides an example of how the balloon drifts over a period of time. As shown in the figure, after 40 minutes, the balloon is at an altitude of 7 km and has traveled 50 km Northeast of its release location at State College, PA.

Theoretically, one calibration constant should be sufficient for all measurements of water vapor by the LAMP lidar, however, the calibration constant is subject to change if there are any changes made to LAMP'S system. For instance, the average visible

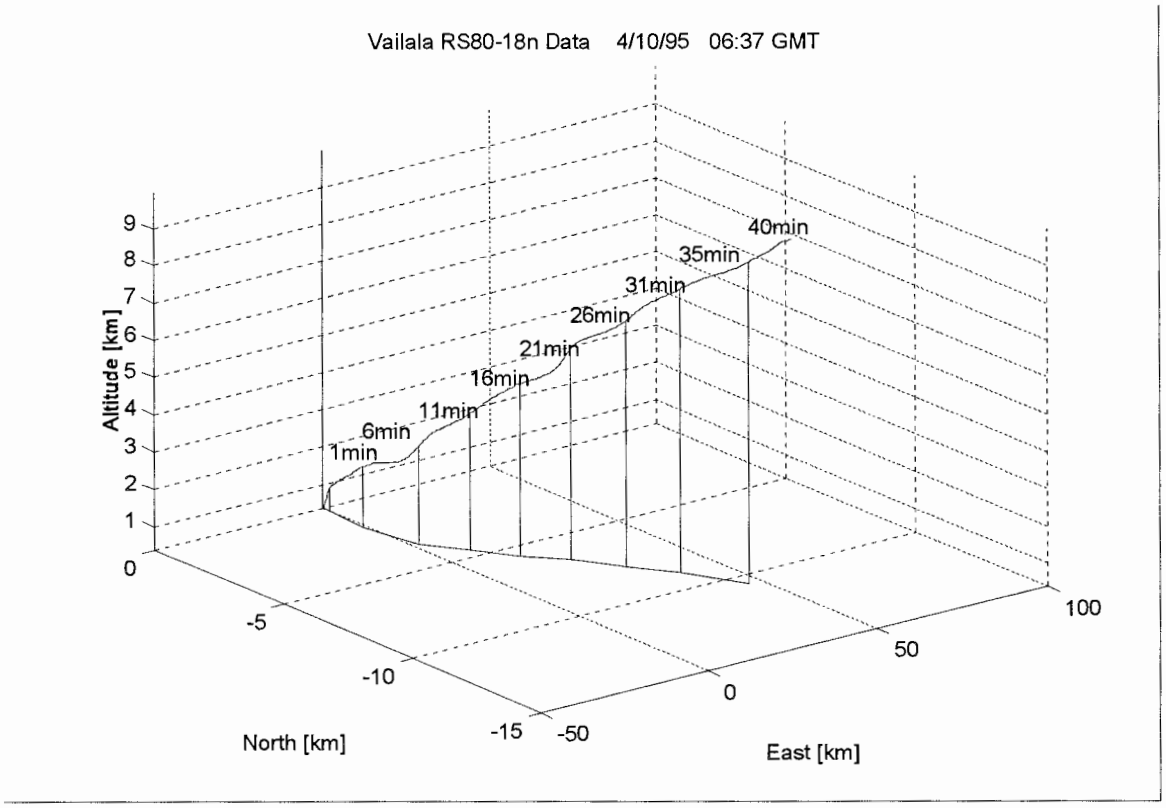

Figure 11. A map of the course a balloon takes after being launched.

visible calibration constant obtained during the CASE I measurement program on Wallops Island is 22 with a 17% uncertainty and the average UV calibration constant is 304 with a 8% uncertainty. This uncertainty was contributed to the fact that LAMP was operating in the vertical mode as well as the horizontal mode, in the same evening, which caused the system to need realignment on a regular basis.

Since radiosondes are reportedly 99% accurate, a comparison of the water vapor measurements obtained by the LAMP lidar and the radiosonde gives a good indication of LAMP's ability to measure water vapor. Figures 12 and 13 display a comparison of water vapor mixing ratio measurements obtained by LAMP and a coincident radiosonde at

Wallops Island on September 18, 1995 at 02:45 UT and September 20, 1995 at 23:52 UT, respectively. LAMP's profiles were integrated over 30 minutes with a 75 m vertical resolution. The other profiles were obtained from radiosonde measurements of temperature and relative humidity. A comparison of the lidar and radiosonde profiles shows that they have similar characteristics, thereby showing that the measurements between both instruments are consistent. For instance, in Figure 12 both the radiosonde and LAMP reveal the same detailed layer structure from the ground to 4 km. Also, in Figure 13, both the radiosonde and LAMP detect the same dry layer starting at 1.3 km.

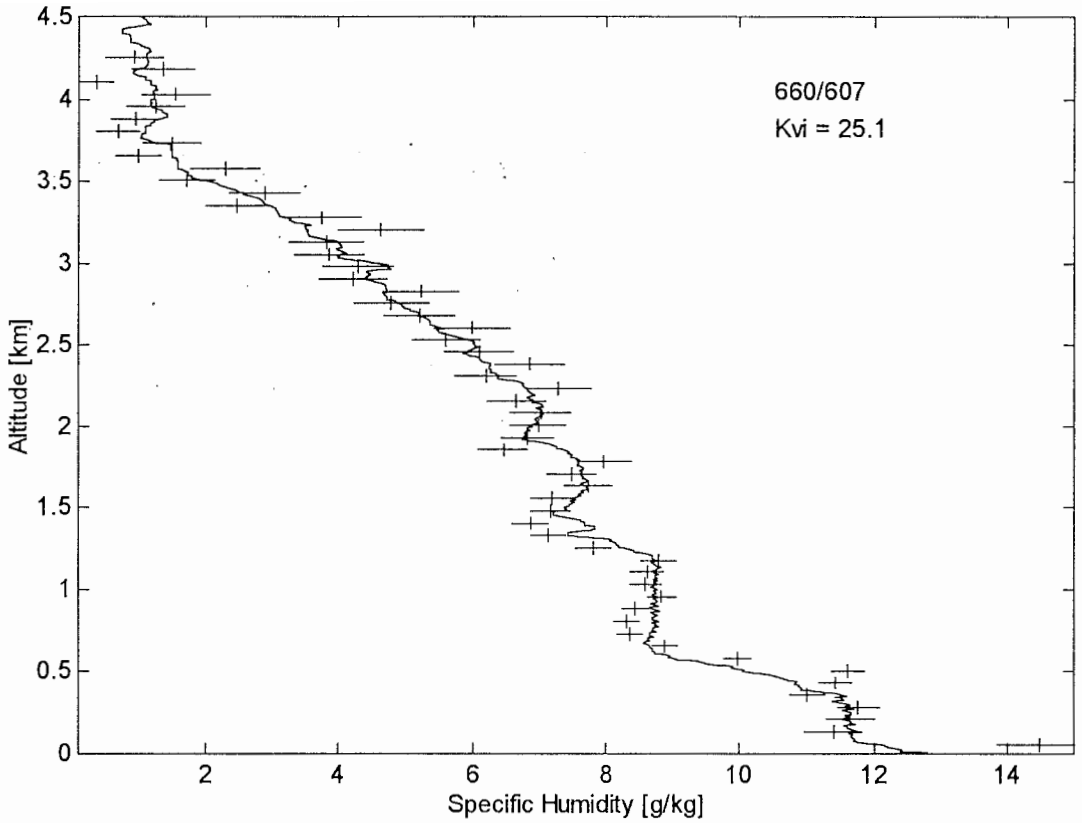

Figure 12. Vibrational Raman lidar water vapor profile together with a concurrent radiosonde profile. {September 18, 1995, 02:45 UT, Wallops Island, VA}

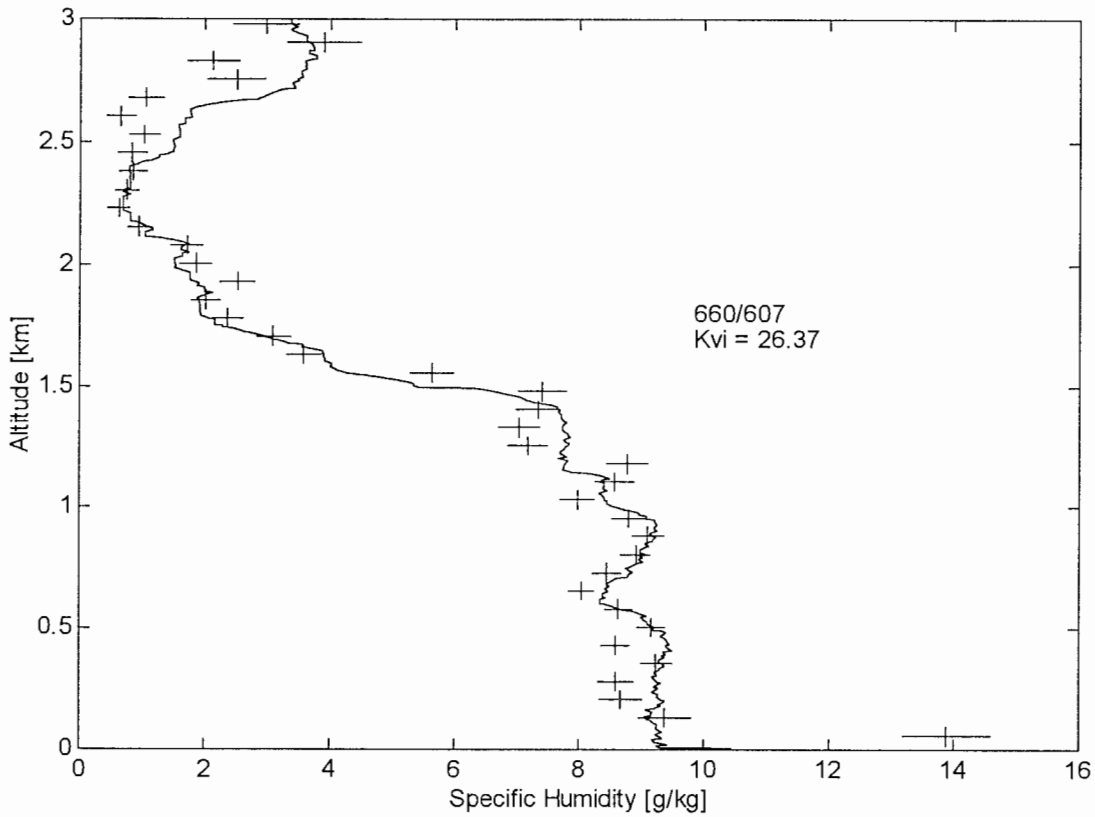

Figure 13. Vibrational Raman lidar water vapor profile together with a concurrent radiosonde profile. {September 20, 1995, 23:52 UT, Wallops Island, VA}

4.3 Comparison of the UV and Visible Channels

The LAMP lidar is capable of measuring the constantly changing water vapor of a column of air that is directly in the line of sight of the laser. Figures 14 and 15 provide examples of water vapor mixing ratio profiles measured by both the visible and UV channels starting at 02:00 UT on September 15, 1995 and beginning at 00:27 UT on September 20, 1995, respectively. The profiles have been integrated for 60 minutes and have a 75 m vertical resolution.

In the first 2 km, the profiles obtained by the UV and visible channels are in good agreement. Upon correlation of the two channels, the correlation coefficient for the data shown in Figures 16 and 17 was found to be 0.98 and 0.93, respectively. The correlation coefficient is not 1.00 because the UV and visible channels are two independent channels that are individually calibrated with the radiosondes, any discrepancies in the calibration of the two channels cause small differences between their measurements.

The comparison of the measurements obtained by both the UV and the visible channels is only valid up about 2.5 km, because the UV channel did not obtain measurements beyond that point. The UV channel is limited because of the low laser output power at 266 nm, the increased atmospheric scattering, and absorption that occurs in the UV region of the spectrum [29]. The 532 nm wavelength is more suitable than the 266 nm for obtaining nighttime measurements of water vapor. As shown in Figure 16, the visible channel was able to obtain useful water vapor measurements up to 5 km. At higher altitudes, data smoothing may be used in order to obtain a more accurate representation of the measured quantity. This technique can be achieved by using the raised cosine

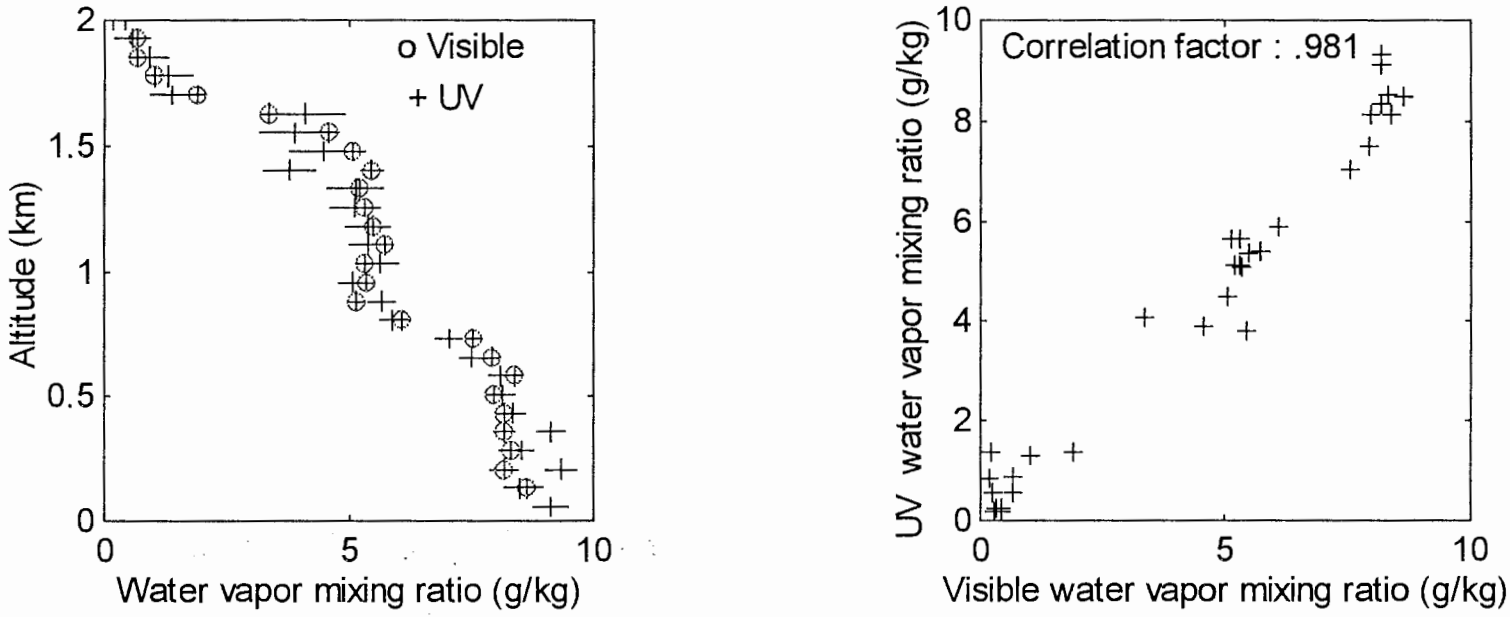

Figure 14. Comparison of water vapor mixing ratio profiles obtained by the visible and UV channels. The right panel shows the correlation between the two, the correlation coefficient is 0.98. {September 15, 1995, 02:00 UT, Wallops Island, VA}

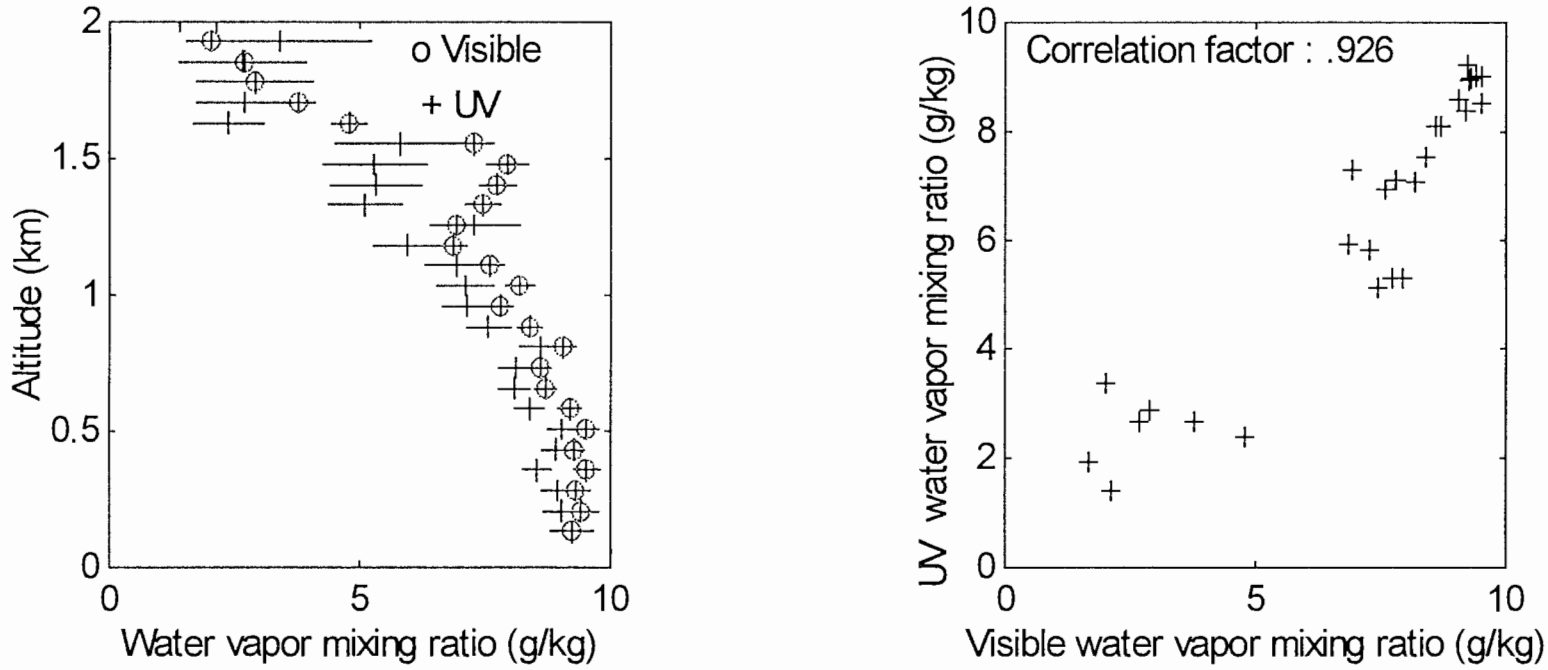

Figure 15. Comparison of water vapor mixing ratio profiles obtained by the visible and UV channels. The right panel shows the correlation between the two, the correlation coefficient is 0.93. {September 20, 1995, 00:27 UT, Wallops Island, VA}

(Hanning) smoothing function [30], which is given by,

$$Hanning\ Filter\ Function = \frac{(1+\cos[\pi/(n+1)])}{2},$$

n is the number of adjacent measurements used. Using this technique increases the number counts on which the statistical error is based, which results in a smaller statistical error. However, smoothing results in decreased resolution, which can effect the rate of change in gradients encountered [28].

The simultaneous measurements of water vapor using the UV and visible channels allows for the comparison of two independent common-volume lidar measurements. This comparison can be used to validate our technique for obtaining water vapor profiles using the UV channel which is needed to obtain daytime measurements.

4.4 Correction of the UV Channel Measurements

In order to obtain accurate water vapor profiles for the UV channel, it is necessary to account for the attenuation of the signal due to both molecular scattering and ozone absorption. The correction term derived to account for the attenuation due to the wavelength dependence of molecular scattering corrects errors up to 6% at 3 km in the UV channel measurements. After this correction has been applied to the measurements, the correction for ozone absorption must be applied. Figure 17 shows vibrational Raman lidar water vapor profiles obtained with the UV channels. The profiles were measured during nighttime operations beginning at 00:27 UT on September 20, 1995. The left figure

has been corrected for ozone absorption and the right figure has not been corrected. As shown in the figure, the uncorrected figure required a 20% correction at 1 km.

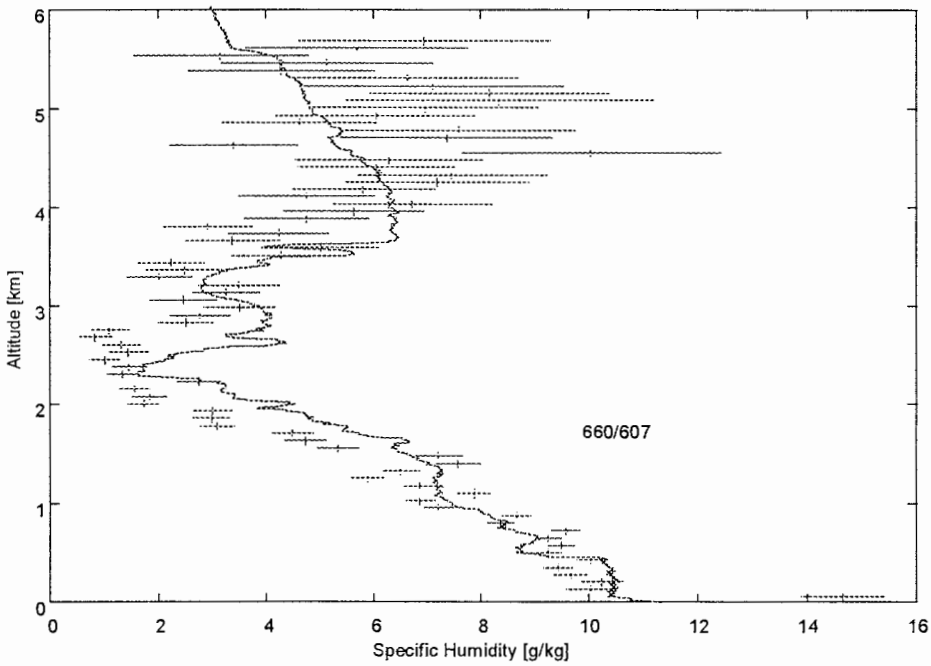

Figure 16. Lidar water vapor profile obtained by the visible channel together with a concurrent radiosonde profile. Measurements were obtained up to 5km. {September 20, 1995, 01:42 UT, Wallops Island, VA}

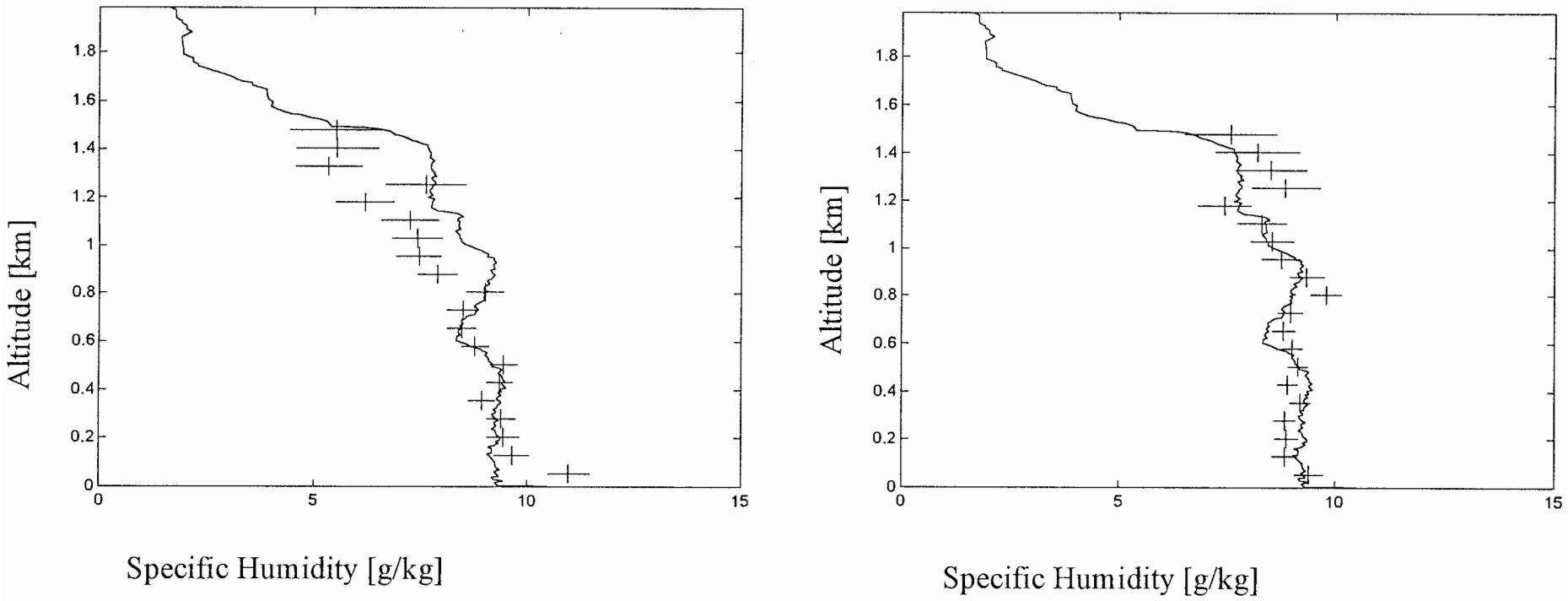

Figure 17. Nighttime vibrational Raman water vapor profiles from the UV channel. The left profile has been corrected for ozone absorption, the right profile has not been corrected. {September 20, 1995, 00:27 UT, Wallops Island, VA}

4.5 Daytime Measurements

Figures 18 and 19 show examples of UV water vapor daytime measurements with concurrent radiosonde profiles. The profiles were obtained on September 20, 1995 beginning at 19:25 UT and 20:13 UT, respectively . The radiosonde was released at 19:38 UT about 3km away from LAMP's site. As shown in the figures, LAMP was only capable of obtaining daytime water vapor measurements up to 1 km. The low range of the lidar is due to misalignment of the laser beam in the field of view of the telescope during daytime operations. Due to the current configuration of the LAMP system, the laser only can be aligned during nighttime operations. As illustrated in Figure 7, the LAMP lidar is mounted on an optical table. Therefore, a slight bump or change in temperature could alter the alignment of the system. The data points in Figures 18 and 19 have large error bars, which are due to the reduced signal from the alignment error and a light leak in the 277 nm filter, which increased the background counts and lowered the signal-to-noise ratio.

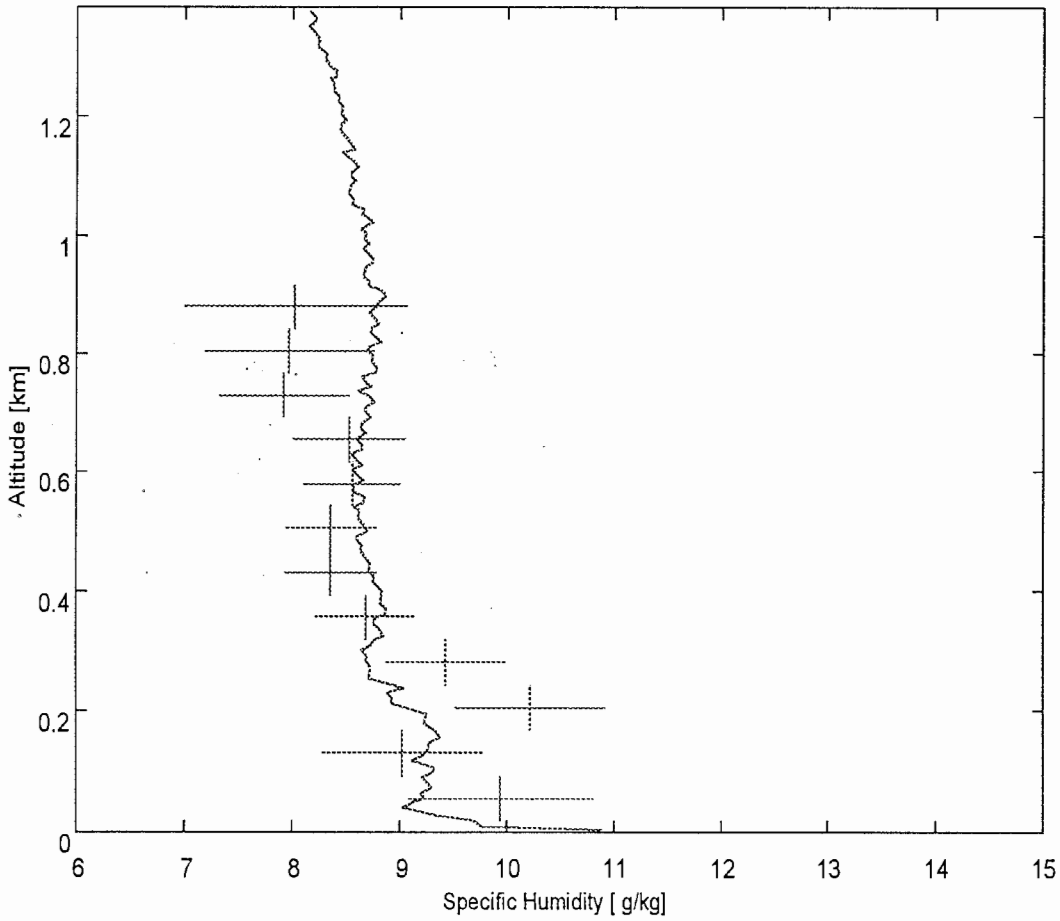

Figure 18. Daytime vibrational Raman water vapor profile from the UVchannel. {September 20, 1995, 19:25 UT, Wallops Island, VA}

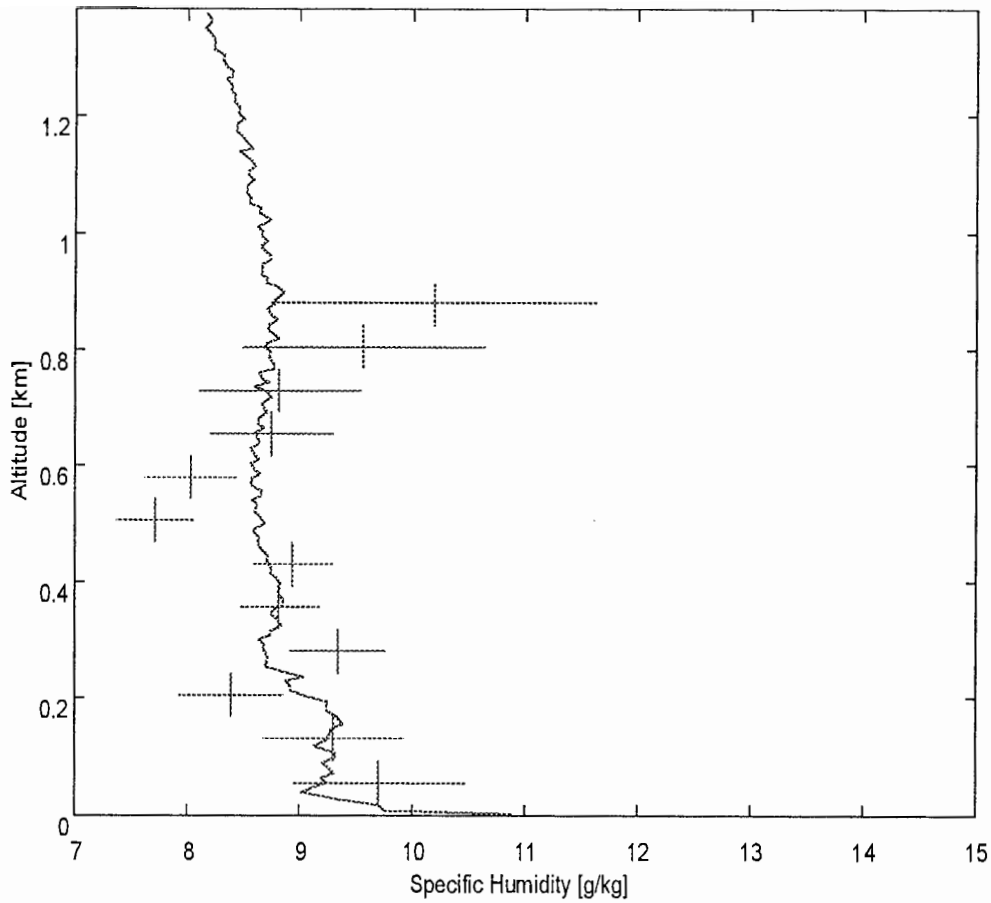

Figure 19. Daytime vibrational Raman water vapor profile from the UV channel. {September 20, 1995, 20:13 UT, Wallops Island, VA}

CHAPTER 5

Conclusions

The Penn State LAMP lidar has proven to be a useful instrument for the study of atmospheric water vapor. The water vapor measurements obtained from LAMP have been demonstrated to be in good agreement with water vapor measurements obtained from radiosondes. However, unlike radiosondes, LAMP's measurements provide water vapor profiles with improved spatial and temporal resolution which allows for the detection of small variations in the water vapor. Therefore, in some instances, LAMP has demonstrated the capability to supplement or even replace radiosondes in gathering measurements of atmospheric water vapor in the lower troposphere.

In Chapter 3, water vapor mixing ratio measurements were displayed, along with the methods of using corrections for the attenuation of the backscattered signal due to molecular scattering and ozone absorption. Using the correction term that was derived to account for the attenuation due to the wavelength dependence of molecular scattering corrects possible errors in the measurements, which for the visible channel is up to 2% at 5 km and for the UV channel is up to 6% at 3 km. Using the correction term that was derived to account for the attenuation due to ozone absorption corrects a 20% error in the UV channel measurements at 1km.

In Chapter 4, a comparison was made of the simultaneous nighttime measurements obtained from the ratio of 660/607 nm obtained from the vibrational Raman returns of a 532 nm pulsed beam and the ratio of 295/285 nm obtained from the vibrational Raman

returns of a 266 nm pulsed beam. The comparison has proven that using the vibrational returns from 266 nm at 295, 284, and 277 nm provides a valid the technique to measure water vapor in the lower troposphere. A comparison of the UV and visible channel produced a correlation coefficient of 0.96. Next, daytime water vapor profiles that were obtained using the vibrational returns from 266 nm at 295, 284, and 277 nm were presented in order to demonstrate LAMP's capability for obtaining daytime measurements of water vapor. Figures 18 and 19 illustrated that LAMP obtained useful daytime measurements of water vapor up to 1 km. However, Figures 12 and 13 show that the UV channels are capable obtaining water vapor measurements above 2 km during nighttime operations. Therefore, the UV channel should be capable of measuring water vapor up to 2 km during daytime operation since the background has been removed by the stratospheric ozone. However, due to the alignment of the system and problems with 277 nm filter, measurements were not obtained up to that altitude in this data set.

5.1 Improving Daytime Performance of LAMP

The LAMP lidar has been collecting data for about 5 years and during that time, it has gone through several upgrades and changes. Several of those changes were made in order to make daytime operations possible. For instance, using the 266 nm output in the solar blind region was intended to provide useable daytime signals. Also, reducing the field of view of the telescope and reducing the filter bandpass of the optical system help to improve daytime performance. Adding an energy monitor to the LAMP system was another attempt to improve the LAMP's daytime performance. The energy monitor

continuously monitors the laser's output energy which is needed in order to obtain the desired signal strength. It was found that the 4th harmonic crystal was temperature sensitive and careful monitoring is required to maintain the laser output at 266 nm. Appendix 1 and the thesis of Sprague [31] provide a full description of a laser energy monitor, which was built and added to the LAMP instrument to support this research effort.

5.2 Future work

A goal of the Penn State lidar group is to develop a lidar that will measure atmospheric properties on a regular basis, unlike the LAMP lidar which is mainly used as a research tool. Thus, using LAMP as a prototype, the LAPS system, Lidar Atmospheric Profile Sensor, has been developed to constantly measure atmospheric properties, such as temperature and water vapor , on board a Naval research vessel. The constant use of the LAP's system requires it to be very rugged. It is designed around a rugged optical table which should maintain the alignment of the system. Also, the signal advantage of LAPS is about 10 times greater than LAMP's, making it possible to increase the range of daytime measurements, obtain a higher SNR, and obtain better range resolution.

References

1. Peixoto, J.P. and A.H. Oort, *Physics of Climate*. New York: American Institute of Physics, 1992.

2. Measures, R.M., *Laser Remote Sensing*. New York: John Wiley & Sons, 1990.

3. Melfi, S.H. and D. Whiteman, " Observations of Lower- Atmospheric Moisture Structure and Its Evolution Using a Raman Lidar," *Bulletin American Meteor. Society*. vol 66, no.10, 1288-1292, 1985.

4. Grant, W.B., *Laser Spectroscopy and its Applications*. New York: Marcel Dekker, 1987.

5. Grant, W. B., "Differential absorption and Raman lidar of water vapor profile measurements: a review," *Optical Engineering*. vol 30, no.1, 40-46, 1991.

6. Elliot, W.P., and D.J. Gaffen. "On the utility of radiosonde humidity archives for climate studies," *Bulletin American Meteo. Society*. vol 72, no. 10, 1507-1520, 1991.

7. Schotland, R.M., "Some observations of the vertical profile of water vapor by a laser optical radar," Proc. 4th Symp. on Remote Sensing of the Environment. University of Michigan, Ann Arbor, 273-283, 1966.

8. Murray, E.R., R.D. Hake, J.E. Van der Laan, and J.G. Hawley, "Atmospheric water vapor measurements with a 10 micrometer DIAL system," *Appl. Phys. Letter*, vol 28, no.9, 542-543, 1976.

9. Rothe, K.W., "Monitoring of various atmospheric constituents using a cw chemical hydrogen/deuterium laser and a pulsed carbon dioxide laser." *Radio Electron Eng.*, vol 50, no. 11/12, 567-574, 1980.

10. Browell, E.V., T.D. Wilkerson, and T.J. Mcllrath, " Water vapor differential absorption lidar development and evaluation." *Appl. Opt.*, vol. 18, no. 20, 3474-3483, 1979.

11. Leonard, D., "Observation of Raman scattering from atmosphere using a pulsed nitrogen ultraviolet laser, *Nature*, vol. 216, 142-143, 1967.

12. Melfi, S.H., "Remote Measurements of the Atmosphere Using Raman Scattering," *Applied Optics*. vol. 11, no. 7, 1605-1610, 1991.

13. Ferrare. R.A., S.H. Melfi, D.N. Whiteman, K.D. Evans, F.J. Schmidlin, and D. O'C. Star, "A Comparison of Water Vapor Measurements Made by Raman Lidar and Radiosondes," *American Meteorological Society*. vol.00, 1-19, 1995.

14. Philbrick, C.R., "Raman lidar measurements of atmospheric properties.", *SPIE*, vol. 2222, 922-931, 1994.

15. Rau, Y.-C., "Multi-wavelength Raman-Rayleigh lidar for atmospheric remote sensing," PhD dissertation, Penn State University, 1994.

16. Stevens, T.D., "An Optical Detection System for a Rayleigh/Raman Lidar." M.S. Thesis, Penn State University, 1992.

17. O'Brien, M.D., *Design of a Data Acquisition and Control System for a Volume Scanning Multi-Wavelength Polarization Lidar*. M.A. Thesis , The Pennsylvania State University, 1994.

18. Kyle, T.G., *Atmospheric Transmission Emission and Scattering*. Terrytown, NY: Pergamon Press, 1991.

19. Stephens, G. L., *Remote Sensing of the Lower Atmosphere*. New York: Oxford University Press, 1994.

20. Ulaby, F.T., *Microwave Remote Sensing, Volume I: Microwave Remote Sensing-Fundamentals and Radiometry*, Norwood, MA: Artech House, 1981.

21. Haris, P., *Pure Rotational Raman Lidar for Temperature Measurements in the Laser Troposphere*. PhD dissertation, Penn State University, 1995.

22. Valley, S.L., Ed., *Handbook of Geophysics and Space Environments*, Air Force Geophysics Laboratory, Springfield, VA, 1985.

23. Rajan S, T.J. Kane, and C.R. Philbrick, "Multiple-wavelength Raman lidar measurements of atmospheric water vapor," *Geophysical Research Letters*. vol. 21, no.23, 2499-2502, 1994.

24. Rees, W.G., *Physical Principles of Remote Sensing*. New York: Cambridge, 1990.

25. Nicolet, M., R.R. Meier, and D.E. Anderson, Jr. "Radiation Field in the Troposphere and Stratosphere II. Numerical Analysis," *Planet. Space Sci.*, vol. 30, no. 9, 935-981, 1982.

26. Renault, D., J.C. Pourny, and R. Capitini, "Daytime Raman lidar measurements of water vapor," *Optics Letters*, vol. 5, no. 6, 233-235, 1980.

27. Bevington, P.R., and D.K Bevington, *Data Reduction and Error Analysis for the Physical Sciences*. McGraw-Hill, New York, 1992.

28. Mckinley, S.C., *Water Vapor Distribution and Refractive Properties of the Troposphere*. M.S. Thesis, The Pennsylvania State University, 1994.

29. Machuga, D.W., *Daytime Performance of the LAMP Rayleigh/Raman Lidar system.* M.S. Thesis, The Pennsylvania State University, 1993.

30. Philbrick, C.R. et al., "Measurements of the High Latitude Middle Atmosphere Dynamic Structure Using Lidar." *AFGL-TR-87-0053 Environmental Research Papers*, no. 867, Hanson AFB, MA, 1987.

31. Sprague, S., *Energy Monitoring and Control of Harmonic Generators for Lidar Applications*. M.S. Thesis, The Pennsylvania State University, 1994.

Appendix

LAMP's Energy Monitor

As a part of my research, I used the design of LAPS' energy monitor developed by Sprague [31] to prepare an energy monitor for LAMP. Figures 20 and 21 illustrate the dimensions and arrangement of the scattering block, filter assemblies, and circuit chassis. The relative size of the circuit chassis actually used is twice as large as those shown in Figures 20 and 21. However, the dimensions of the filter assembly and scattering block remain the same. For a detailed description of the energy monitor see Sprague [31].

Figure 22 displays the final peak detector circuit for LAMP's energy monitor. The first component in the circuit is a photodiode. Since the energy monitor is separated into two channels for measurements at 532 nm and 266 nm, a different diode was used for each channel. The HUV-1100BQ from EG&G was chosen for the visible channel. However, since the spectral range of the HUV-100BQ did not include 266 nm, the MRD510 made by Motorola was chosen for the UV channel. The first operational amplifier, an OPA606, provides high input impedance for the detector circuit. The 3.3 μf capacitor charges until the input voltage reaches a peak, however, when the input falls, the 1N914 low leakage diode prevents the capacitor from discharging. The 100 kΩ resistor serves as a 'bleed' resistor, its value was chosen so that the droop rate and slew rate objectives were met [31]. An operational amplifier serves to amplify the signal and to

provide low output impedance to the circuit. It also provides a high impedance for the capacitor, in order to prevent the capacitor from discharging too quickly. Resistors R1 and R2 are determined by the amount of gain needed. The second diode prevents any bias currents from the second op-amp from reaching the capacitor.

The objective of the energy monitor is to provide a voltage that is linearly proportional to the optical power. As a final test of the energy monitor, its output was calibrated against a power meter. Figure 23 includes data taken from the energy monitor and a power meter at 266 nm. A least squares fit has been applied in order to demonstrate the linearity of the energy monitor.

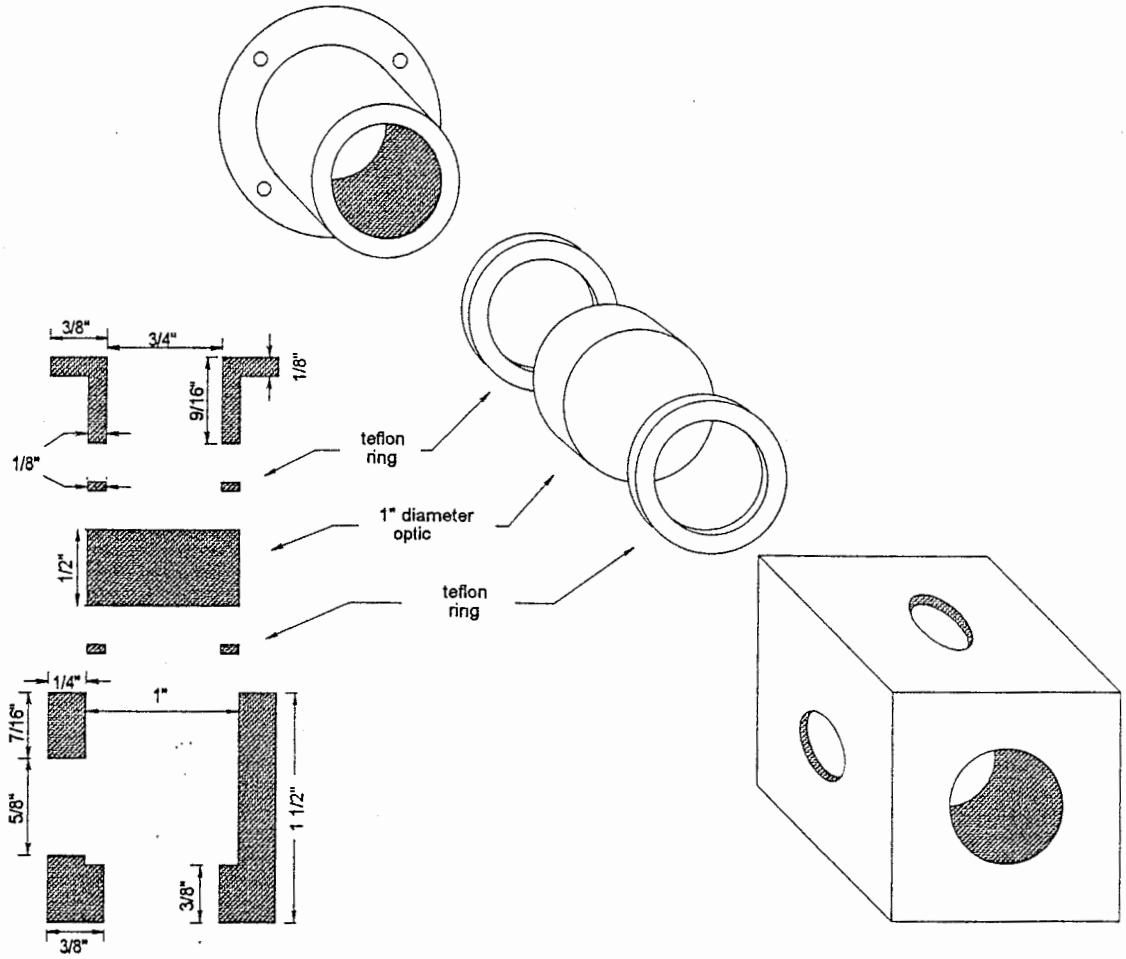

Figure 20. Energy monitor scattering block design, (Sprague, 1995 [27]).

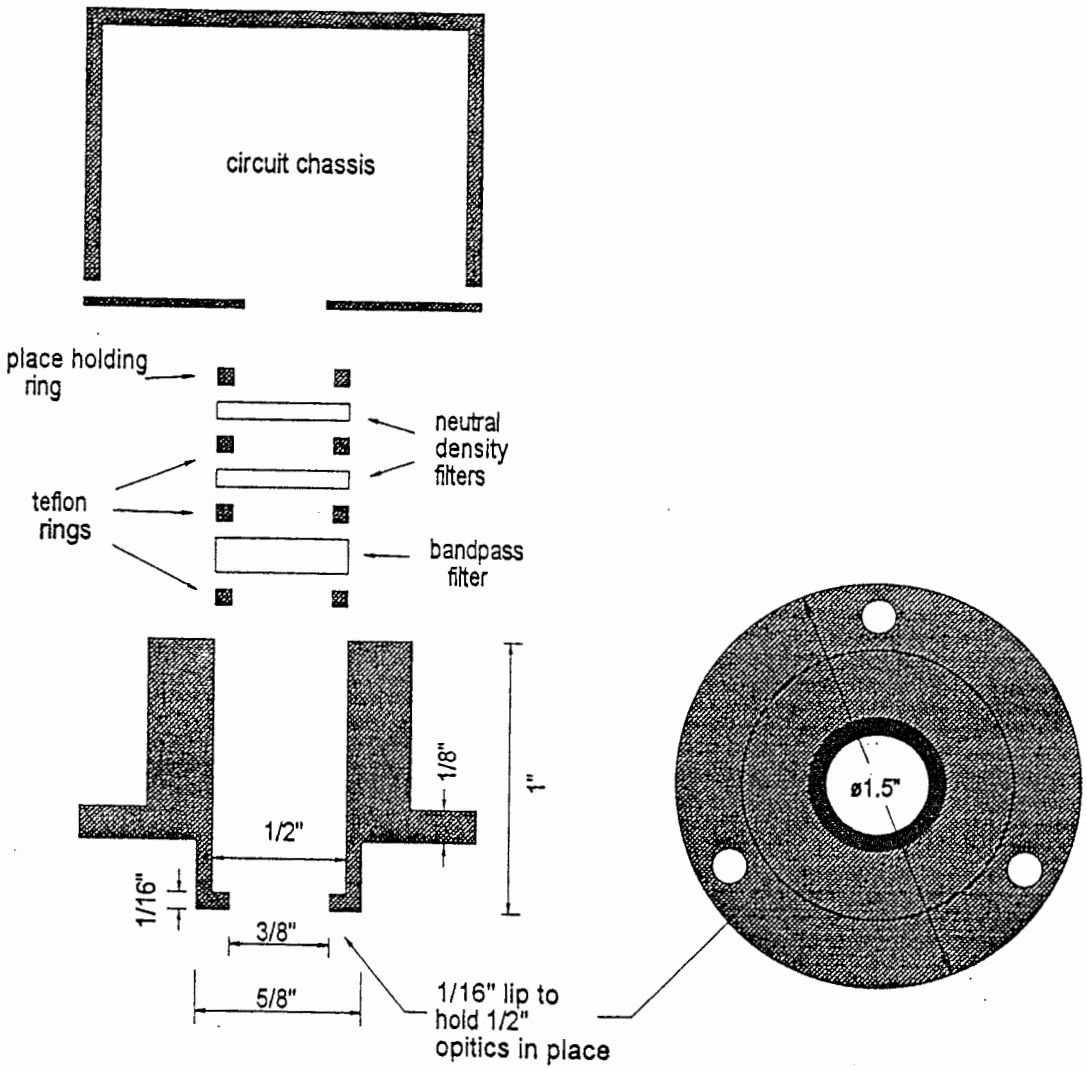

Figure 21. Energy monitor filter assembly design (Sprague, 1995 [27]).

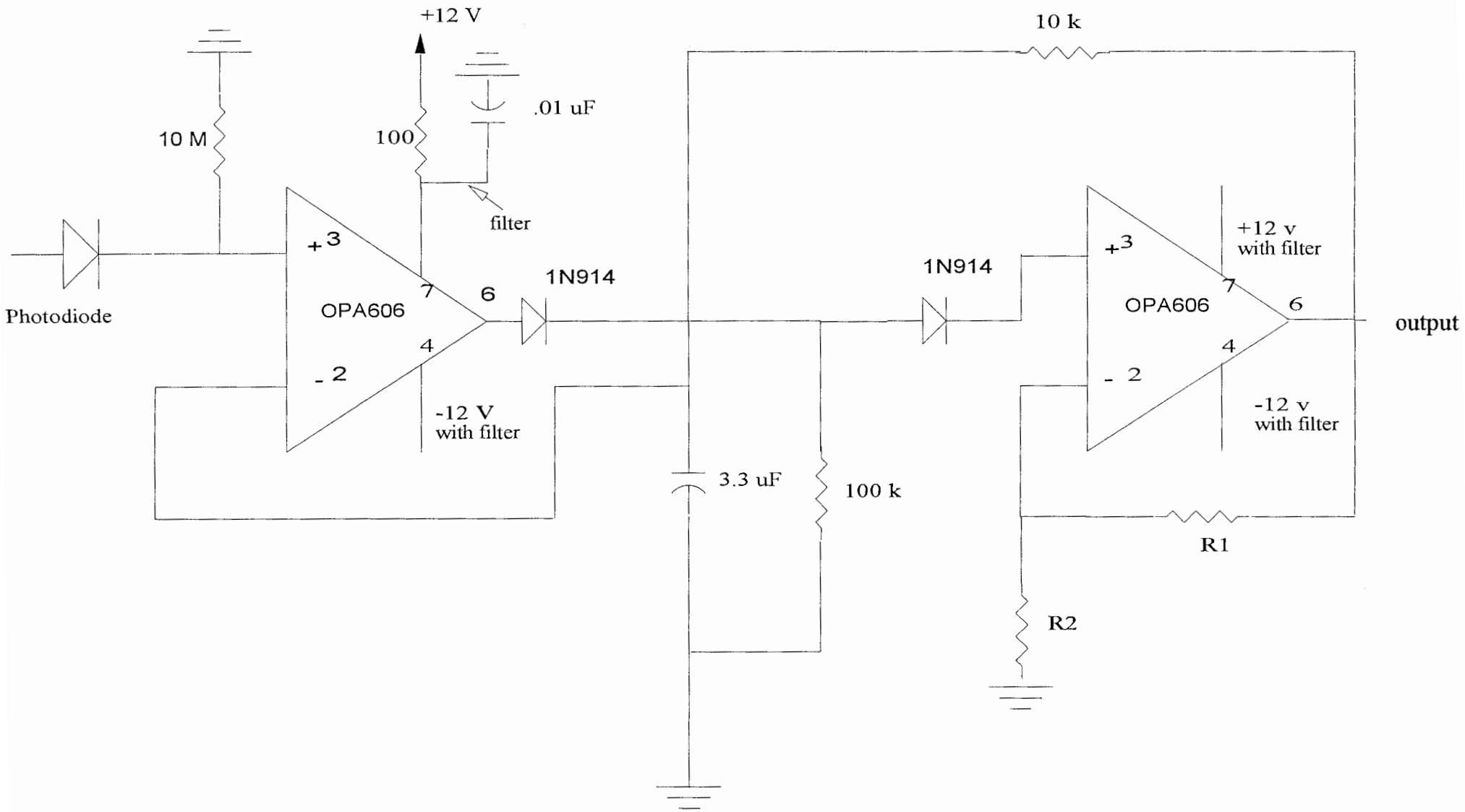

Figure 22. Circuit design for LAMP's energy monitor.

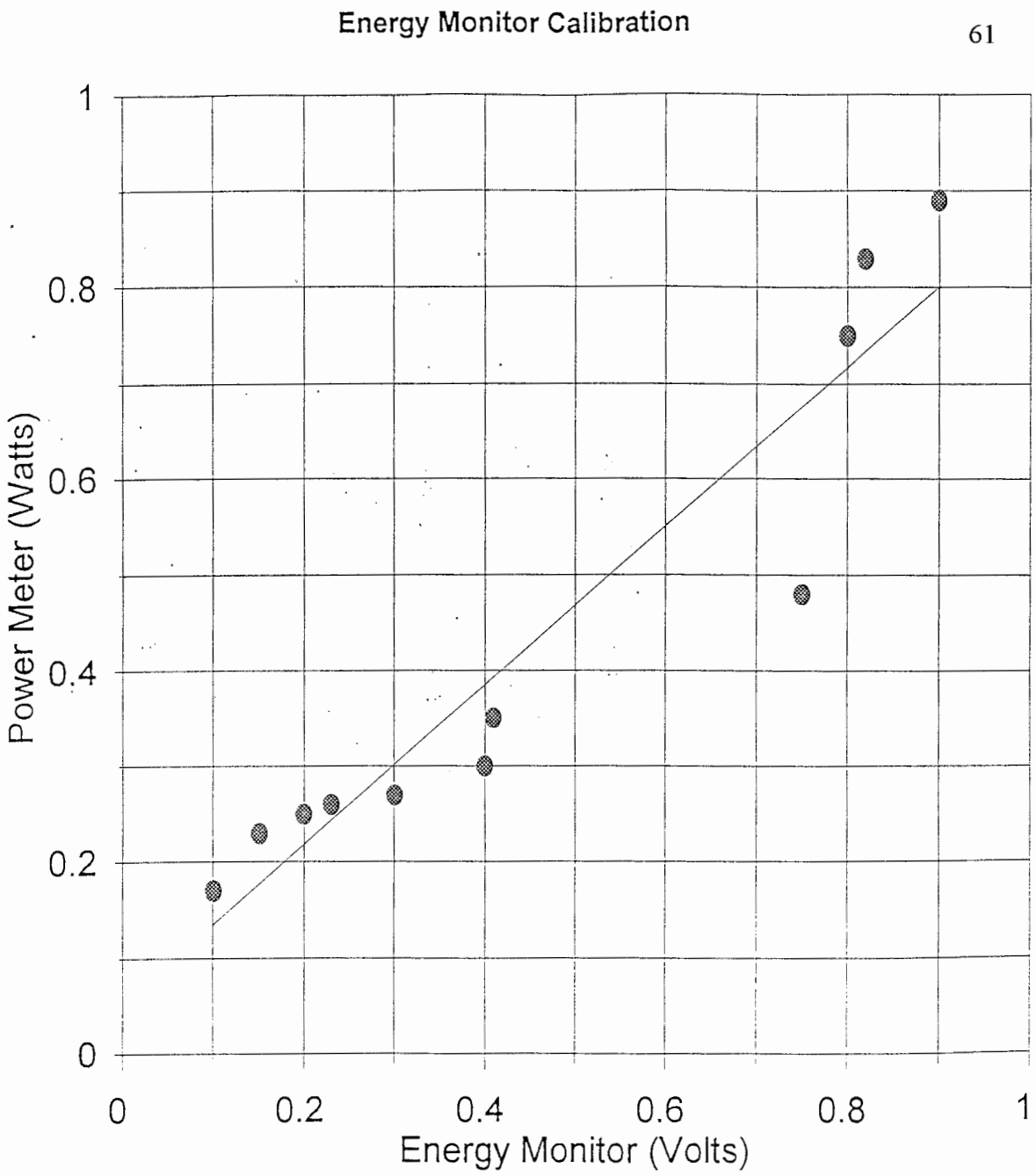

Figure 23. Calibration of energy monitor versus power meter at 266 nm.